Title

Approved by
Supervising Committee:

Supervisor Name (no title), Supervisor

2nd Reader Name (no title), Supervisor

Dedication

Your words here.

Acknowledgements

Your acknowledgements here.

Date

Abstract

Title

Your Official UT Name, Previous Degree

The University of Texas at Austin, 2000

Supervisors: Supervisor Name and Second Reader Name

Abstract text here.

Table of Contents

List of Tables

List of Figures

Fatigue Strength of Fillet-Welded Transverse Stiffeners With Undercuts

by

Joseph Richard Spadea, B.S.C.E.

Thesis

Presented to the Faculty of the Graduate School of

The University of Texas at Austin

in Partial Fulfillment

of the Requirements

for the Degree of

Master of Science in Engineering

The University of Texas at Austin

May 2002

Fatigue Strength of Fillet-Welded Transverse Stiffeners With Undercuts

Approved by
Supervising Committee:

Karl H. Frank

Michael D. Engelhardt

Dedication

To my parents and grandparents Salvato, John and Mike for their encouragement and love throughout my academic studies.

To my late grandparents Vincent and Barbara Spadea, for their fortitude and perseverance in realizing the American Dream.

Acknowledgements

This thesis is based on research sponsored by the Texas Department of Transportation for the Center for Transportation Research at the Phil M. Ferguson Structural Engineering Laboratory at the University of Texas at Austin.

I would like to express my sincerest thanks to my advisor Dr. Karl H. Frank, for it was an honor and privilege learning from him. I am very grateful for his guidance, advice, and friendship throughout the research project. I would also like to thank Dr. Michael D. Engelhardt for his time and suggestions in reviewing this thesis.

To Blake Stasney, Mike Bell, Dennis Fillip and Ray Madonna for their technical expertise and assistance in the laboratory. Thank you for your efforts and time when I needed it most. The results of this thesis would not be possible without their insight and willingness to lend a helping hand.

Lastly, I would like to thank my colleagues, the fine students of the structural engineering department. You truly are the backbone of our prestigious program and your friendship will be valued throughout my lifetime.

May 2002

Abstract

Fatigue Strength of Fillet-Welded Transverse Stiffeners With Undercuts

Joseph Richard Spadea, M.S.E.

The University of Texas at Austin, 2002

Supervisor: Karl H. Frank, Michael D. Engelhardt

Steel girders are subjected to cyclic loading caused by the impact of vehicular traffic on a daily basis. Poorly detailed stiffener attachments will result in fatigue cracking of the girder. The effect of wrapping the stiffener-to-flange weld upon the fatigue life was evaluated. The impact of undercuts at the stiffener clip and flange edge upon fatigue strength was also determined. Several test specimens were developed including a stiffener detail with no clip opening. It was found that wrapping the welds around the stiffener had no impact upon the fatigue life of the specimens.

Table of Contents

List of Tables

List of Figures

CHAPTER 1
Introduction

1.1 INTRODUCTION

Steel girders are subjected to cyclic loading caused by the impact of vehicular traffic on a daily basis. In stiffened girders, repeated flexure places the stiffener connection to the flange in cyclic tension. Poorly detailed stiffener attachments will result in fatigue cracking of the girder. An overview of several stiffener details is discussed in this chapter. In particular, the welding procedure used to attach the stiffener to the flange is explored. A literature survey and a worldwide survey of bridge fabrication techniques included in this chapter reveal the state-of-the-art in stiffener detailing. The scope and objective of the research contained in this thesis are included in this chapter.

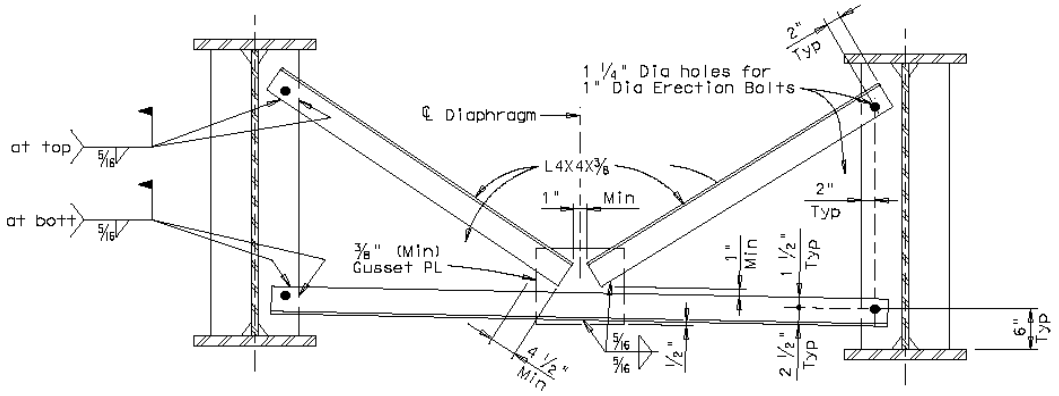

Figure 1-1: Girder Diaphragm (TxDOT)

Fillet welds are used in the fabrication of steel bridge girders to connect the ends of transverse stiffeners to the flange. *The AASHTO LRFD Bridge Design Specifications* (2nd Edition, 1998) requires this connection on compression flanges

to control distortion of the web-to-flange intersection. The stiffener must also be connected to the tension flange when a cross frame or diaphragm is connected to the stiffener. The diaphragms are typically attached to the stiffener as shown in Figure 1-1. Diaphragms are mainly used during construction to provide lateral bracing to the girder during the erection process. The stiffeners are run the full depth of the girder web and are welded directly to the flanges. The lateral forces from the diaphragm will cause fatigue cracks to form in the web at the end of stiffener weld if the stiffener is not welded to the flange. Some states use a bolted rather than a welded connection between the stiffener and the flange. Two angles are welded to the stiffener and bolted to the flange. The two details are shown in Figure 1-2.

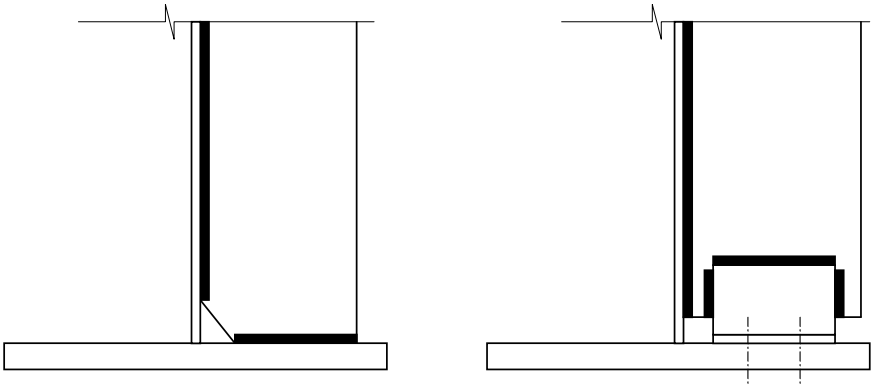

Figure 1-2: Stiffener-to-Flange Connections

The welded detail is the preferred detail since it does not require fabrication and fitup of the angles and the drilling of the flange bolt holes. The Texas Department of Transportation (TxDOT) uses the welded detail. Termination of the fillet welds at the end of the stiffener has been a subject of much discussion. The present AASHTO welding specification does not require the wrapping of the welds around the end of the stiffener. Historically, these welds were required to be wrapped to seal the weld in order to prevent corrosion

at the interface of the stiffener and flange. Undercutting at the corner of the stiffener often caused the wrapped welds to be rejected and subject to grinding to feather out the undercut. The current specification language prohibits wrapping of the welds to prevent the undercutting but leaves the ends of the stiffener exposed to moisture. Some states require sealing of the ends with caulking, which is difficult to perform and not a long-term solution. The current stiffener-to-flange weld detail used by The Texas Department of Transportation is shown in Figure 1-3.

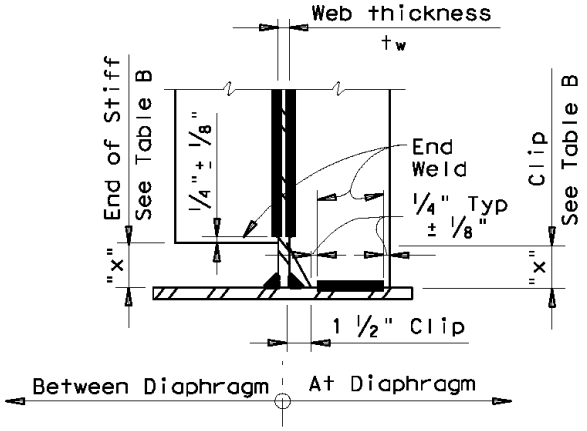

TABLE B	
Web Thickness tw	"X" ⑧
5/16" to 3/8"	1 1/2"
Over 3/8" to 5/8"	2 1/2"
Over 5/8" to 1"	4"

⑧ The fabricator may use an "X" different from what is shown provided that the following is satisfied: $4t_w \leq$ "X" $\leq 6t_w$

Figure 1-3: Current Stiffener Weld Detail (TxDOT)

The influence of wrapping the weld upon fatigue performance was evaluated through experimental testing at Ferguson Structural Engineering Laboratory. Undercutting of the corners of stiffeners is unavoidable. In addition, undercutting of the flange edge may occur if the width of the stiffener is large. Undercuts at the corner of the flange are more likely to reduce fatigue performance than undercuts of the stiffener. The impact of undercutting the corners of the stiffener and flange upon fatigue performance were determined and are presented in this thesis.

The wrapping of the welds at web side of the stiffener is difficult since it must be performed through the clip. A large clip may be required to provide access for the welder. A large clip reduces the amount of weld that can be placed which may lead to weld failures from the cross frame forces. Elimination of the clip and allowing the intersection of the stiffener and web-to-flange fillets welds is a possible alternative. Testing of stiffener details with and without a clip were conducted.

1.2 FABRICATION SURVEY

A recent Federal Highway Association sponsored worldwide survey of steel bridge fabrication revealed that most countries wrapped the stiffener weld. Findings from this survey are summarized in the FHWA report titled *Steel Bridge Fabrication Technologies in Europe and Japan* (Verma et al, 2001). It was found that other countries use a small clip on the stiffener and fill the void with weld metal sealing the weld and eliminating the need to wrap the weld inside the clip. A photograph of this stiffener detail is shown in Figure 1-4. Note that the weld is also fully wrapped at the flange edge side of the stiffener and that good weld profile was maintained with minimal undercutting.

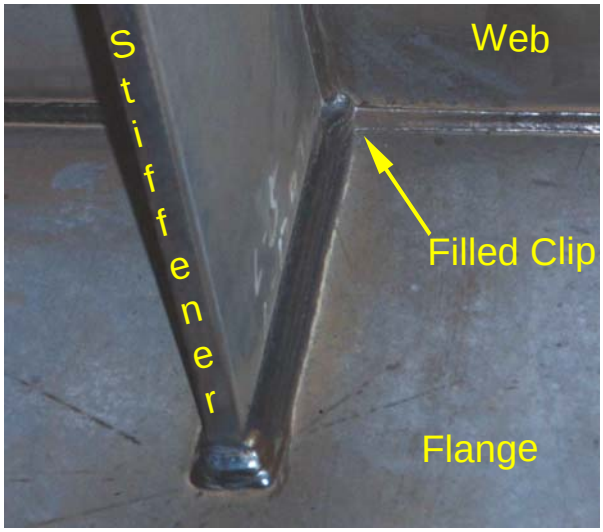

Figure 1-4: Fully Wrapped Stiffener, No Clip

Intermediate and cross-frame stiffeners are shown on the girder in Figure 1-5. Fabricators wrapped the welds around the interior clip space near the web on the diaphragm stiffener. The edge of the diaphragm stiffener near the flange was also sealed. In addition, the stiffener-to-web weld of the intermediate stiffeners was also wrapped around the top and bottom of the attachment.

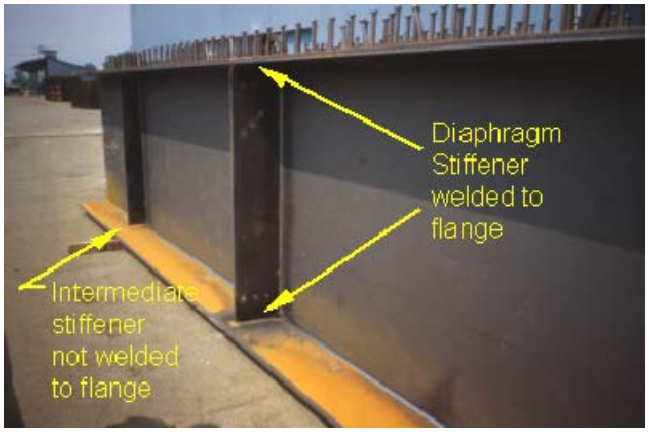

Figure 1-5: Girder in Fabrication Yard

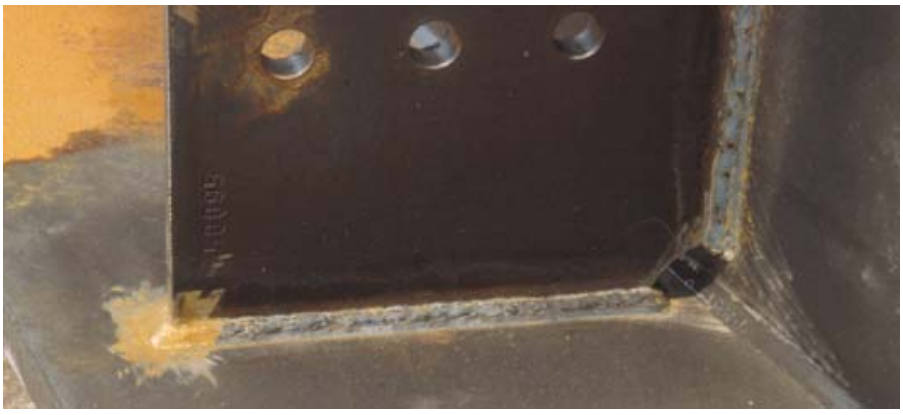

Figure 1-6: Fully Wrapped Diaphragm Stiffener

Figure 1-7: Wrapped Intermediate Stiffener Welds

Figure 1-6 shows a close-up view of the diaphragm stiffener weld detail. It can be seen from the figure that a circular “mouse hole” clip was used to fitup the stiffener to the web. TxDOT uses a straight clip detail (refer to Figure 1-3). Notice also that the weld shape and profile are maintained along the length of the stiffener, including the wrapped edges. The holes shown in the stiffener are used to bolt the diaphragm to the stiffeners during erection.

Figure 1-7 shows a close-up view of the intermediate stiffener weld detail. The web-to-stiffener welds were carefully wrapped around the top and bottom edges of the stiffener. It should be noted that the stiffeners were welded to the web prior to the attachment of the flanges. The stiffener-to-flange weld shown in Figure 1-6 was made last.

1.3 LITERATURE SURVEY

Ruge and Woesle tested three different stiffener details in cyclic four-point bending at 11 Hz. The stiffener detail was located in the constant moment region and tested at a stress range of 17 ksi (117 MPa) at the extreme fiber of the tension flange. The stress range is defined as the difference between the upper and lower stress limits at the extreme tension fiber during testing.

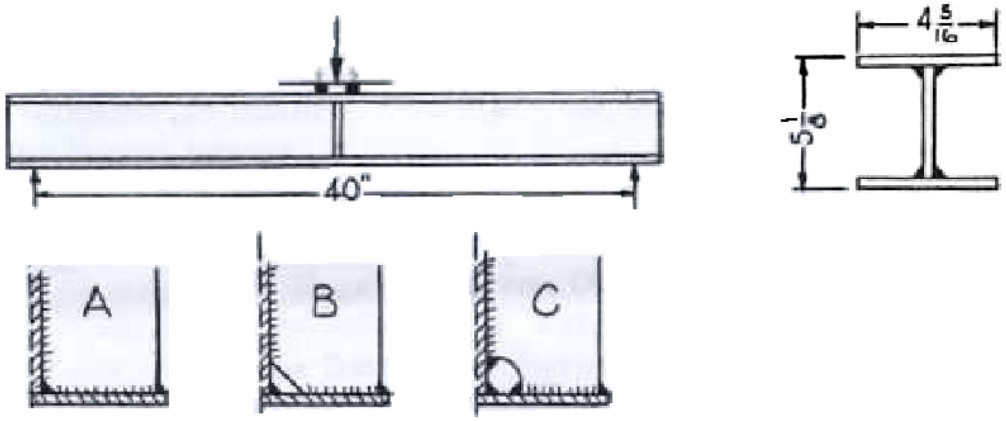

Figure 1-8: Specimen and Setup (Ruge and Woesle, 1962)

Figure 1-8 shows the specimen geometry and test setup used by Ruge and Woesle. Dimensions are given in inches in Figure 1-8. Stiffener details A through C were connected to the flange using 0.125 in. (3 mm) fillet welds. Stiffener A has no interior clip opening, and welds were used to seal the stiffener to the web and flange. It should be noted that the stiffener-to-flange weld did not seal the interior stiffener clip for detail B. Ruge and Woesle indicate that stiffener detail B is at a disadvantage since water can infiltrate between the stiffener and flange leading to corrosion. However, detail C uses fully wrapped welds at the interior clip region. Welds appear to be wrapped around the flange edge of the stiffener for all specimens A through C.

It was reported that all cracks occurred along the toe of the stiffener-to-flange weld. In addition, no cracks initiated at the web-to-flange weld in the stiffened beams. Stiffener detail B was used to investigate the effects of crater cracks on the fatigue performance of the beams. Ruge and Woesle concluded that the crater cracks did not impact the fatigue life of the beams. Failure of the type B stiffened beams occurred due to fatigue cracking at the toe of the stiffener-to-flange weld.

Another significant conclusion drawn by the authors was that weld sequence did not impact the fatigue performance of the specimens. The results of the fatigue testing performed by Ruge and Woesle are perhaps the most significant findings in relation to the research presented in this report. It will be shown in Chapter 4 that the specimens tested at Ferguson Structural Engineering Laboratory also failed due to crack growth at the toe of the stiffener-to-flange welds.

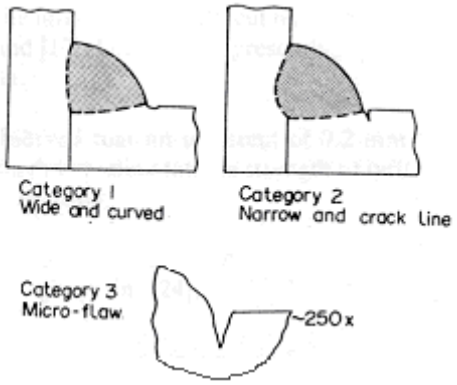

Figure 1-9: Types of Undercuts (Petershagen, 1990)

The Influence of Undercut on the Fatigue Strength of Welds – A Literature Survey (Petershagen, 1990) provides an in-depth discussion on the geometric variables of undercuts at the toe of fillet welds and butt welds and their impact on fatigue life. In the survey, an undercut is described as an "irregular groove along

the toe of a weld." Petershagen adds that the undercuts are inherent in the welding process and may occur in either the base or fill metal. Three classifications of undercuts are shown in Figure 1-9. Type one undercuts are referred to as "wide and curved." Category two undercuts are "narrow", and category three undercuts are considered "micro-flaws", with a depth less than 0.01 in. (0.25 mm). Category three undercuts are believed to be unavoidable during welding and impossible to detect by visual inspection.

Petershagen's survey also indicated that undercuts are generally characterized by their length, height, and width. In addition, the transverse orthogonal plane angel, ρ, and the notch root radius, r, were used to describe the geometry of an undercut. Figure 1-10 illustrates several dimensions used to represent the geometry of undercuts. However, it was found that only the length, height, and direction of principal stresses are considered in AWS D1.1 and German Shipbuilding Production Standard.

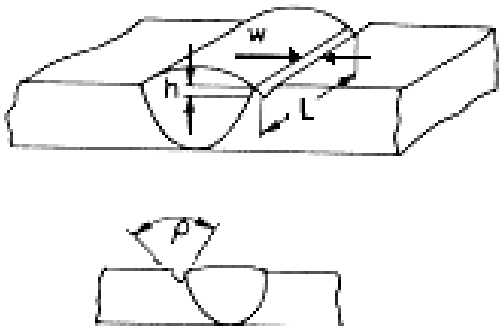

Figure 1-10: Undercut Dimensions (Petershagen, 1990)

Wrapping welds around gusset ends may increase the size of undercuts (Petershagen, 1990). The author describes that wrapping fillet welds around non-load bearing gussets attached to a plate yielded an average undercut height of 0.02 in. (0.49 mm). The unwrapped fillet weld produced average undercut depths of 0.006 in. (0.15 mm). Similar results may occur in the wrapping of stiffener-to-

flange welds around the edge of non-load bearing stiffeners connected to flange plates.

Inspection of type one undercuts can be made using calipers or silicon prints (Petershagen, 1990). Petershagen reports that type two undercuts are best inspected using dye penetrant testing and magnetic particle testing. Type three undercuts will also require the use of 250:1 scale microscopes. For the purposes of the research conducted at Ferguson Structural Engineering Laboratory, undercuts were exaggerated to produce "worst-case" undercuts. Thus, undercuts were visible and measured using calipers to an accuracy of $\pm$0.005 inches.

Petershagen discusses the impact of undercuts on fatigue performance. It was found that the fatigue life of welds with initial crack-like flaws could be readily calculated using fracture mechanics equations. The fatigue life of welds with type one or type two undercuts can also be determined. However, Petershagen adds that no literature includes the simultaneous effects of type one, two, and three undercuts.

Petershagen suggested that non-dimensional values, such as h/t (height-to-thickness ratio), be used when describing undercuts. In addition, Petershagen states that the crack initiation period is independent of the undercut depth, h. It was also found that type one undercuts may cause a small impact on the fatigue life of butt-welds, and that shape of fillet welds has a more significant impact on fatigue life than undercutting (Petershagen, 1990).

Influence of the shape of undercut on the fatigue strength of fillet welded assemblies – application of the local approach (Janosch and Debiez, 1998) evaluated the impact of weld shape and continuous and discontinuous undercuts at the fillet weld toe on fatigue strength. The authors state that the fatigue resistance of structural details is based on nominal loads and plate thickness.

They add that design codes do not consider the fatigue strength as a function of weld quality or undercutting.

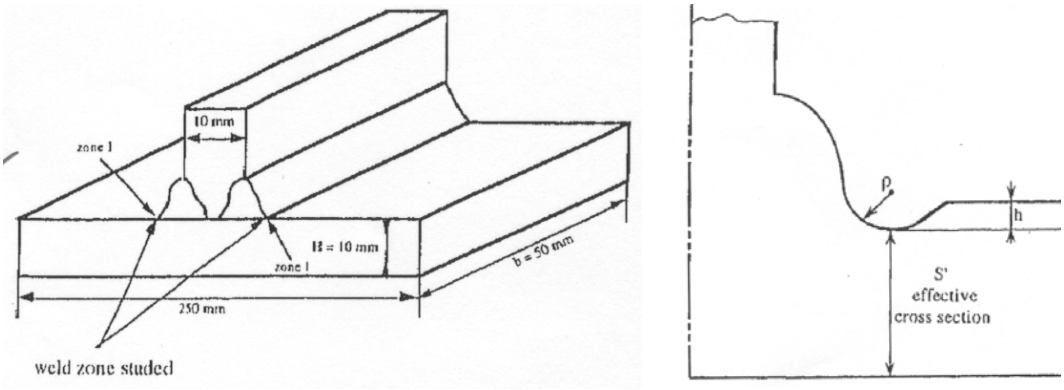

Figure 1-11: T-Joint and Undercut Geometry (Janosch and Debiez, 1998)

Janosch and Debiez tested specimens welded by the manual and MIG/MAG processes. Four weld undercutting geometries were examined: (1) continuous undercuts at the upper toe by manual welding with covered electrodes in the flat position; (2) discontinuous undercuts at the upper toe by manual welding with covered electrodes in the flat position; (3) discontinuous undercuts at both toes by manual welding with covered electrodes in the vertical upward position; and (4) continuous undercuts at the upper toe by MIG/MAG welding with solid wire in the flat position. T-shaped assemblies like the one shown in Figure 1-11 were tested in four-point bending at 20 Hz to 40 Hz and a stress ratio of 0.1. The stress ratio is defined as the minimum applied stress divided by the maximum applied stress.

The geometry of the undercuts is also shown in Figure 1-11. The undercuts are characterized by toe radius, ρ, and undercut depth, h. Table 1-1 shows the mean and standard deviation of these parameters per weld geometry 1 through 4 as measured by Janosch and Debiez.

Janosch and Diez also performed statistical data reduction analyses using nominal stress amplitude and an effective nominal stress amplitude. The effective nominal stress amplitude was based on the effective cross-section, S', shown in Figure 1-11. These analyses provided the authors with equiprobability curves related to fatigue life as a function of the experimental results.

Table 1-1: Undercut Measurements (Janosch and Debiez, 1998)

Welding Geometry	Radius ρ (in.)		Depth h (in.)	
	Mean	Std. Dev.	Mean	Std. Dev.
1	0.047	0.030	0.029	0.013
2	0.045	0.022	0.010	0.011
3	0.043	0.023	0.011	0.008
4	0.055	0.029	0.016	0.011

The authors have concluded that the size of the root radius is independent of the welding process (SMA or MIG/MAG) and position. As a result of the nominal stress amplitude analysis, they found that covered electrodes in the flat position provided a higher fatigue life than the MIG/MAG process. The effective nominal stress amplitude analysis showed that welding process, position, and undercutting had no significant influence on the effective endurance limits of the test specimens. The local approach showed that the endurance limit was not impacted by weld shape and undercutting.

In *Fatigue Strength of Fillet Welded Joints with Undercuts* (Onuzuka et al, 1993), the authors present the results and findings of test specimens with 0.012 in., 0.02 in., and 0.04 in. (0.3 mm, 0.5mm, and 1.0 mm) undercut depths. The authors tested the specimens in both tension and three-point bending. The test specimens are shown in Figure 1-12. Specimens were assembled using shielded metal arc welding and tested at a stress ratio of 0.1.

Weld toe bead shapes and flank angles (what's a flank angle?) were measured using silicon prints. Onuzuka et al found that there was up to a 30% decrease in fatigue life for specimens with larger undercuts at the weld toe. Flank angles were found to have minimal influence on fatigue performance.

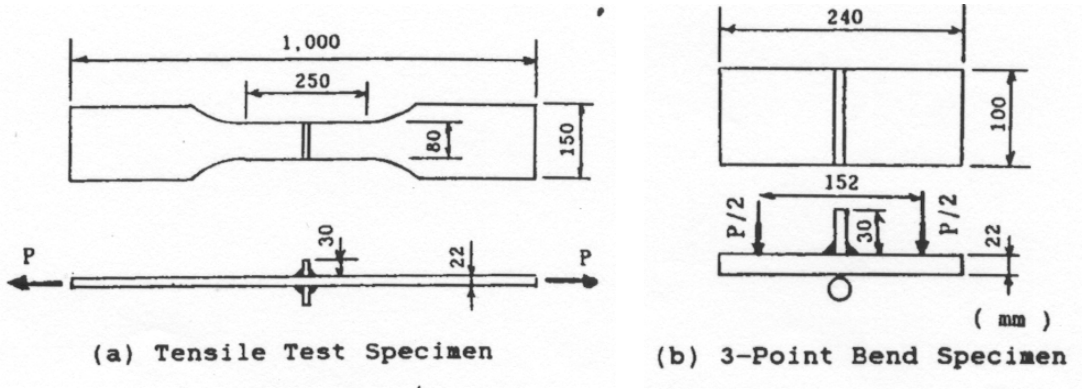

Figure 1-12: Cruciform and Tee Joint Specimens (Onuzuka et al, 1993)

In addition to the experimental results, stress concentration factors and crack growth equations were developed for assemblies with undercuts using the boundary element method. The authors calculated the fatigue life of welded assemblies with undercuts. They found that the fatigue life generated by the analysis for assemblies with 0.04 in. (1 mm) undercuts gave a lower fatigue life than the experimental results. However, the authors found that the fatigue life estimates were similar to test results for specimens with shallower undercuts. The tee joint specimens suffered a decrease in fatigue life proportional to the depth of undercutting (Onuzuka et al, 1993). The authors conclude that the calculations appeared to estimate the fatigue life of the specimens fairly well, yet several assumptions were made and some factors were neglected.

Fatigue Strength of Butt-Welded Joint With Undercut (Iida et al, 1998) compares the results of visual inspections performed by certified inspectors to that of control measurements. The authors were interested in determining a tolerance

level for undercuts as judged by the certified inspectors. In particular, focus was placed on finding an acceptable depth for undercutting. Butt-welded specimens were also tested in fatigue and the authors reported that undercutting has an impact on fatigue life.

0.8 in. (20 mm) butt welds and 0.5 in. (12 mm) fillet welds were used to assemble the specimens using the shielded metal arc welding process (Iida et al, 1998). Weld gauges and silicon replicate prints were used to measure the undercuts on the specimens. Next, over 100 certified inspectors were asked to measure the same undercuts using a 0.1 mm pitch gauge. The inspectors were directed to approve or disapprove by considering not just undercut depth, but overall weld quality. The authors reported that the mean undercut depth measured by the inspectors was lower than the control measurements made with the weld gauge. The inspected butt weld undercuts were found to be 0.006 in. (0.16 mm) smaller than the control measurements. Inspected fillet weld undercuts were found to be 0.002 in. (0.06 mm) smaller than the control measurements. The authors found an error range of +0.004 in. to –0.008 in. (+0.1 mm to –0.2 mm) in measured versus inspected undercut depths. In addition, the authors report that most of the inspectors considered a 0.008 in. (0.2 mm) undercut to be acceptable and a 0.04 in. (1.0 mm) undercut to be unacceptable.

Fatigue tests of butt-welded specimens with undercuts were performed at a frequency of 5 Hz to10 Hz at a zero stress ratio in tension. Specimens with 0.63 in., 1.2 in., and 1.6 in. (16 mm, 30 mm, and 40 mm) plate thickness values were tested. Results showed that the fatigue life decreased with undercut depth. In particular, as the ratio of undercut depth to plate thickness (d/t) increases, the fatigue life decreases. The authors reported a 5%, 10%, and 20% decrease in fatigue life related to d/t ratios of 0.005, 0.01, and 0.02.

Iida et al concluded that inspectors underestimated the undercut depths. In addition to finding that larger d/t ratios reduce fatigue life, the authors added that the decrease was more prominent in thicker plates. The authors proposed the following guidelines for the acceptance of undercuts in butt welds: (1) $d \leq 0.2$ mm for $t \leq 10$ mm; (2) $d/t \leq 0.02$ for 10 mm $< t \leq 40$ mm; (3) $d \leq 0.8$ mm for $t > 40$ mm. The authors believed that using a weld gauge was the best way to measure undercut depths because of the simplicity of the device.

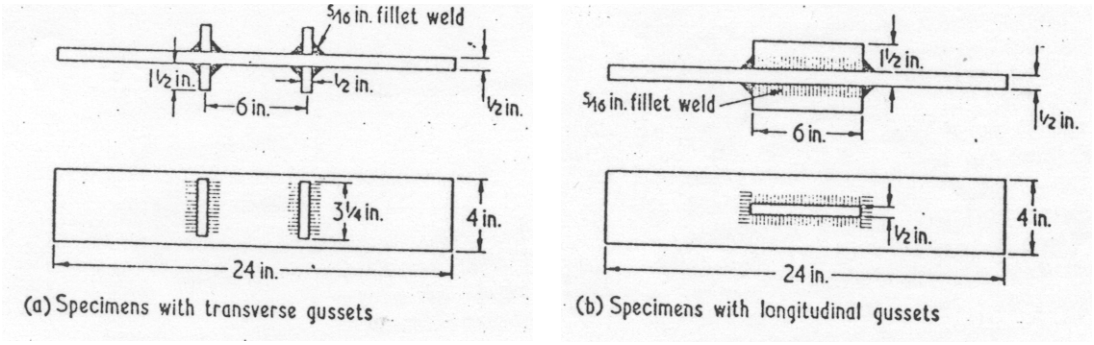

Figure 1-13: Transverse and Longitudinal Specimens (Gurney, 1968)

Methods used to improve the fatigue life of fillet-welded assemblies are discussed in *Effect of Peening and Grinding on the Fatigue Strength of Fillet Welded Joints* (Gurney, 1968). Peening and grinding effects at the ends of transverse and longitudinal fillet welds are investigated using the specimens shown in Figure 1-13. The main plate of the specimens was 0.5 in. in thickness. Peening, partial grinding of the weld toe, and full grinding of the weld were carried out. Specimens were manually welded using E 317 rutile electrodes in the flat position. Welds were fully wrapped around the edge of specimens with longitudinal gussets in some cases. Welds were not wrapped around the edge of the specimens with transverse gussets. Cyclic loading of the specimens took place at a frequency of 3 Hz to 33 Hz and a stress ratio of either 0.0 or -1.0.

Three test machines were used, thus accounting for this variation in frequency and stress ratio.

Gurney concluded that the fatigue performance of the specimens with longitudinal gussets with wrapped welds were the same as for those with unwrapped welds. However, the author adds that there was a particular case where this was not so. Gurney states that a specimen with a longitudinal gusset and wrapped welds failed earlier than the unwrapped gussets. Gurney mentioned that this was due to an undercut at the toe of the weld wrap. Failures of the longitudinal gussets occurred at the weld root. Full-penetration welds were then tested and it was shown that an increase in fatigue strength occurred. However, Gurney also noted that poor quality full penetration welds at the end of the gusset plate could severely decrease fatigue life.

It was found that full grinding of the transverse welds resulted in a 50% increase in fatigue performance. Light grinding was shown to produce mixed results. The author believed that, while fatigue strength increased in some cases, the ability to reproduce the desired light grinding was unreliable. Light grinding depths could be too deep or too shallow and were considered inconsistent. In addition, when fully ground specimens were also peened, a further increase in fatigue performance was shown.

On the Practical Use of Weld Improvement Methods (Nussbaumer and Imhof, 2001) investigates the influence of weld grinding, remelting, and peening. These improvements are applied to the weld toe of welded assemblies to improve their overall fatigue performance. The authors develop adjustments that account for these weld improvements that can be applied to the nominal fatigue resistance categories of Eurocode 3. It was stated that the weld improvements were influenced by the stress ratio, R, and that the corrections work best for low stress ratio values. Although undercuts can be removed by grinding, good weld quality

was also emphasized in order to produce a satisfactory fatigue performance. Nussbaumer and Imhof believe that grinding, peening, and remelting of welds using a TIG torch can not only be applied to new fabrications, but to structures exhibiting cracking less than 2 mm in depth.

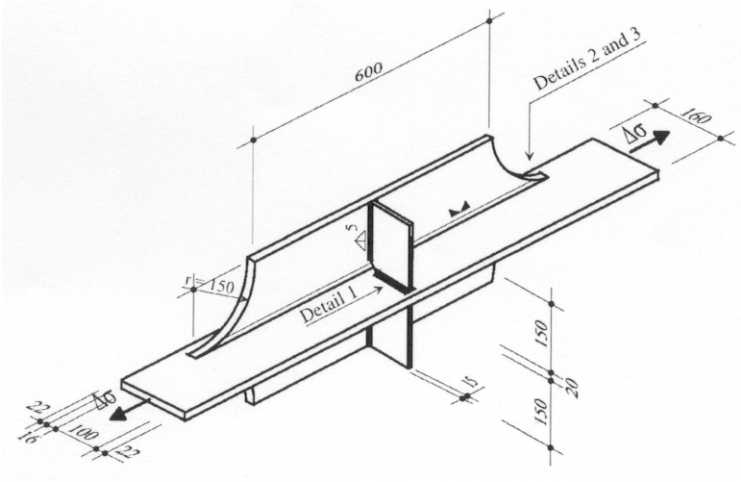

Figure 1-14: Transverse Specimen (Nussbaumer and Imhof, 2001)

Figure 1-14 shows the test specimen used by Nussbaumer and Imhof. Measurements are given in millimeters in the figure. 17 of these specimens were tested at a stress ratio of 0.1. The weld toe of each gusset attachment was treated by peening. In addition a radius was placed at the ends of the larger gusset attachment by using full penetration welds at the radial appendix as illustrated in Figure 1-15. The appendix was then ground tangent to the base plate using a disc grinder. The authors emphasized that grinding striations should be finished parallel to the direction of applied stress as shown in Figure 1-14. Grinding should continue into the base metal to eliminate undercuts caused by the full penetration welding. The rest of the gusset was connected using fillet welds. In addition to this specimen, two full-scale girders with stiffeners attached to the web and flange were tested. The girders were tested in four-point bending with the stiffener attachments located in the constant moment region of the beam.

Some of the findings in the work by Nussbaumer and Imhof coincide with the fabrication of the specimen used for the research in this report. It will be shown that the test specimen discussed in Chapter 2 is similar to the test specimen used by Nussbaumer and Imhof.

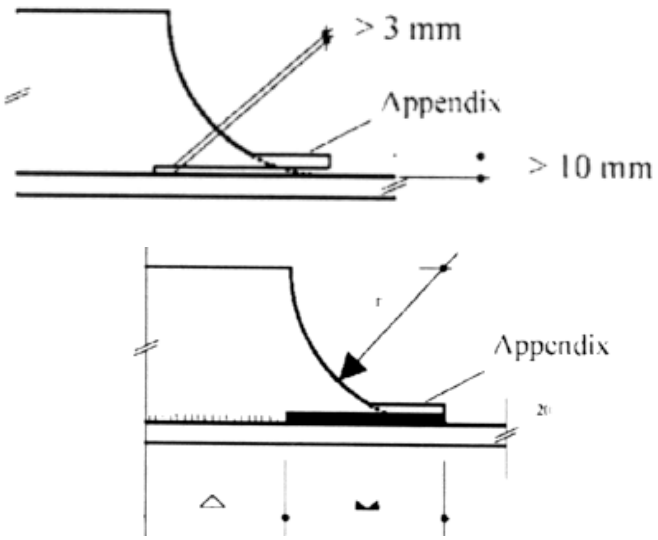

Figure 1-15: Fabrication of Specimen Taper (Nussbaumer and Imhof, 2001)

Nussbaumer and Imhof also suggested that care should be taken at the startup and termination points of the fillet welds. This concept is also discussed in *Fatigue of Welded Structures, 2nd Edition* (Gurney, 1979). Gurney states that termination points in otherwise continuous welds should be ground to a smooth transition and then rewelded. This process is shown in Figure 1-16. Weld start-stop regions are discussed in the following chapter for the fabrication of the test specimens presented in this thesis. Weld start-stop repairs were made by grinding and remelting by a TIG torch.

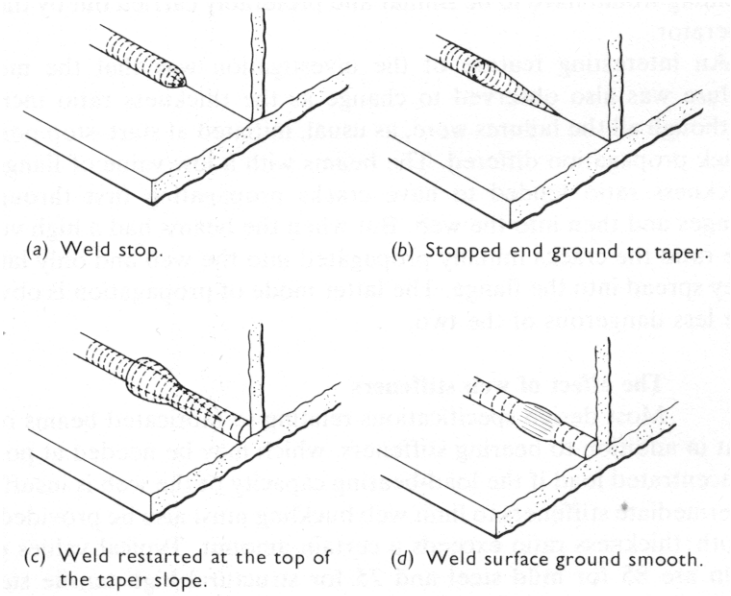

Figure 1-16: Weld Start-Stop Repair (Gurney, 1979)

Nussbaumer and Imhof concluded that design curves could be adjusted using the formulation presented in their work. The authors also emphasized the importance of quality control during welding, namely the weld quality and procedure. They state that the application of the repair procedures should be done so with care and precision. Nussbaumer and Imhof reported that peening improves fatigue strength when lower stress ratios are used.

1.4 SCOPE OF WORK

Limited testing has been conducted on the fatigue strength of stiffeners with undercuts. The literature survey reveals that the focus of research has been on undercutting at the weld toe, and not at the stiffener and flange edge weld wrap locations.

The impact of wrapping the stiffener-to-flange weld upon fatigue life was evaluated and the results are presented in the following chapters. Several test specimens were developed. The fabrication and design of the test specimens are covered in Chapter 2 of this thesis. Undercuts were measured and the values are presented.

Specimens were subjected to cyclic loading in tension. The test apparatus and test procedure are discussed in chapter 3. Strain readings were also compared to a finite element model used in the development of the test specimen. The results of the fatigue tests are given in Chapter 4. Photographs of fatigue cracks and fracture surfaces are included. A data analysis was also performed and included in Chapter 4.

The conclusions of the research presented in this thesis are discussed in Chapter 5. It was found that wrapping the welds around the stiffener had no impact upon the fatigue life of the specimens.

CHAPTER 2
Specimen Design and Fabrication

2.1 INTRODUCTION

The specimens tested during the project are introduced in this chapter. This chapter describes the design process used for the development of the test specimen. Fabrication of each specimen group is covered in detail.

Figure 2-1 shows a steel girder subjected to flexure. The stiffener is welded to both flanges and along the web. Repeated flexure of the girder places the stiffener-to-flange connection under cyclic tensile loading. The stiffener-to-flange detail is highlighted with a circle in the section figure.

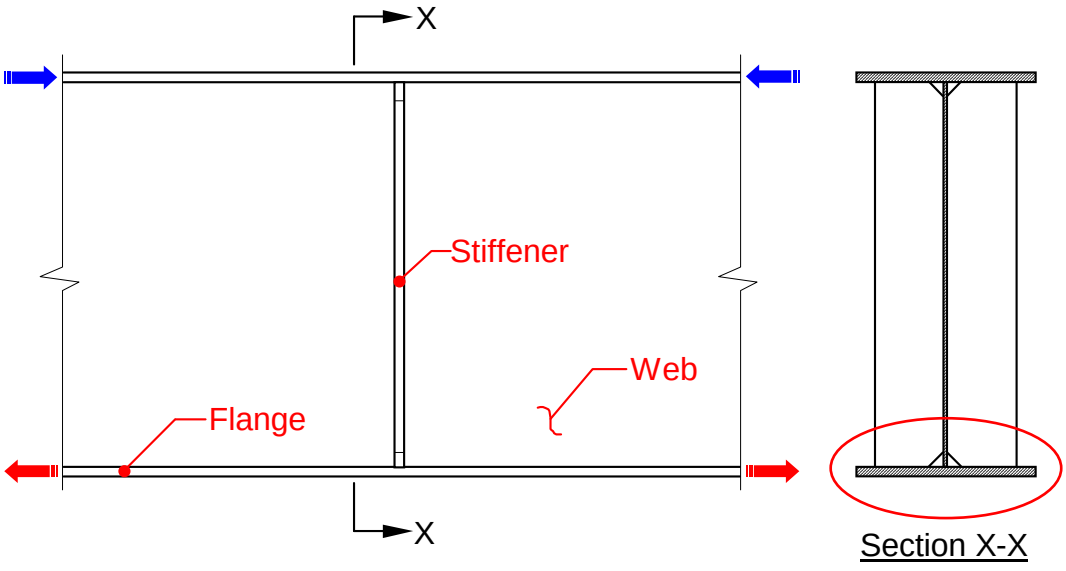

Figure 2-1: Steel Girder and Stiffener Detail Under Flexural Loading

An axially loaded test specimen was used to simulate the tensile stresses in the flange due to girder flexure. The test specimen is shown in Figure 2-2. The

specimen was subjected to axial tensile cyclic loading as illustrated in Figure 2-2. The specimen is symmetric about the flange to ensure uniform stress at the stiffener detail. There are two stiffeners and one web on each side of the flange plate.

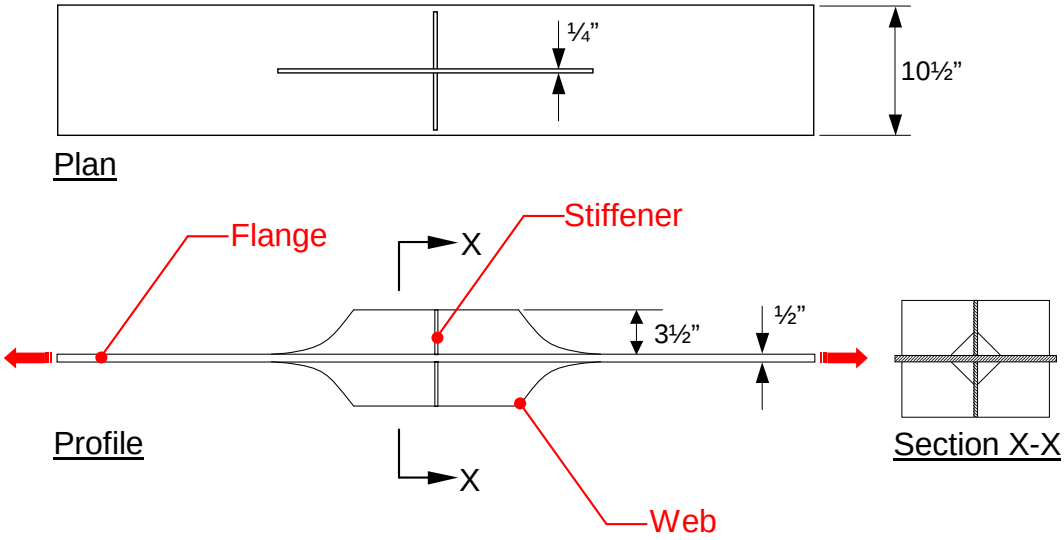

Figure 2-2: Test Specimen Showing Components and Cyclic Loading

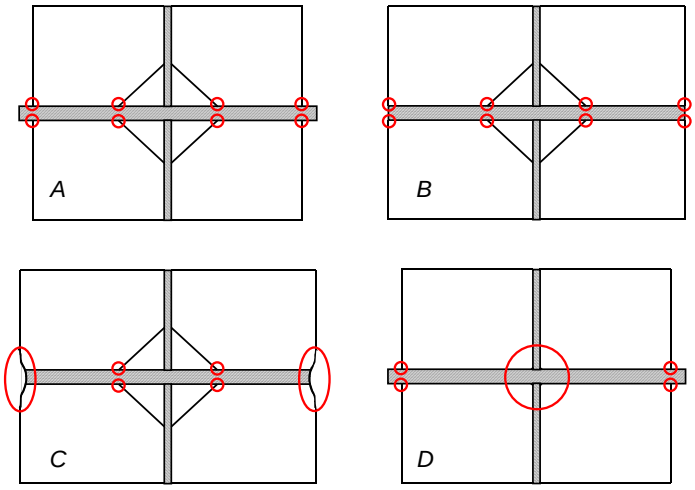

Figure 2-3: Specimen Cross-Section Geometry and Undercut Locations

Four different types of specimens were used to investigate the possible effects of the undercutting caused by wrapping the fillet welds around the stiffener. These specimens, designated type A through type D, were designed to evaluate the fatigue performance based on undercutting at the interior stiffener clip weld wrap and undercutting at the edge of the stiffener-to-flange weld. Figure 2-3 illustrates the cross-section geometry at the stiffener-to-flange connection. Undercut locations and other points of interest are highlighted with circles in the figure. The different specimen types are also shown in Figure 2-4.

Figure 2-4: Photo Showing Variety of Specimens

The type A specimen was used to investigate the impact of undercuts at the interior stiffener clip weld wrap and exterior end weld wrap upon the fatigue life of the specimen. The clear distance between the edge of the stiffener and the edge of the flange was 0.625 in. (16 mm). The type B and type C specimens are the same as type A, but both have a longer stiffener extending completely to the edge of the flange. Specimen types B and C were used to observe undercutting

effects at the interior clip weld wrap and the stiffener-to-flange edge weld wrap. The type C specimen is identical to type B with the exception that the flange edge undercut was removed by grinding after fabrication in accordance with section 3.2.3 of the D1.5-95 Bridge Welding Code (1995). Lastly, the type D specimen was used to investigate the impact on the fatigue life caused by minimizing the clip size and completely welding this area closed. The clear distance between the edge of the stiffener and the edge of the flange was 0.625 in. (16 mm) for type D specimens.

AASHTO LRFD Bridge Design Specifications, 2nd Edition (1998) nominal fatigue resistance categories were employed in the design of the specimens based on a nominal stress range, S_R, of 20 ksi (138 MPa) at the stiffener-to-flange connection. The design ensured that failure of the specimens occurred at either the undercuts or the weld at the stiffener location. The specimens were designed to avoid premature fatigue failure at a location other than at the stiffener detail.

Figure 2-5 shows the dimensions of specimens A, B, C, and D. All specimens were 60 in. long (1524 mm) and had a flange thickness of 0.5 in. (12.7 mm). The stiffener and web plates were each 0.25 in. thick (6.35 mm). The table in Figure 2-5 lists the stiffener width and clip size for each specimen type. The clip is the triangular opening on the stiffener nearest to the web-to-flange weld. The stiffener widths were either 4.5 in. (114 mm) or 5.125 in. (130 mm) and the clip sizes were either 1.5 in. (38 mm) or 0.375 in. (9.5 mm). The specimens were welded using the gas metal arc welding (GMAW) process with a metal-cored electrode. The specimens were assembled using 0.25 in. welds (6.35 mm). The web sections were ground smooth at the ends using a disk grinder to eliminate fatigue cracking at the termination of the weld. The surface grinding marks were finished parallel with the direction of loading.

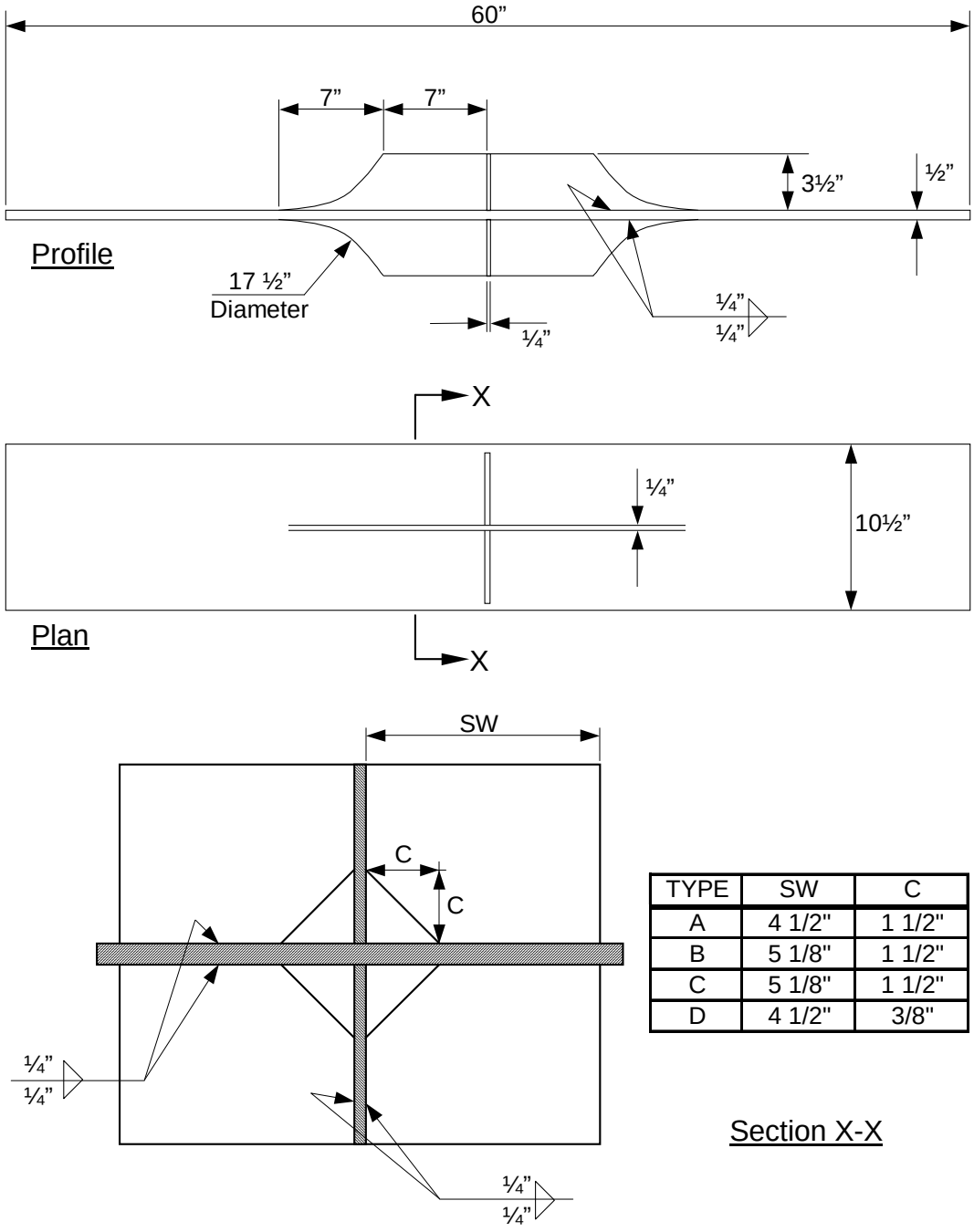

TYPE	SW	C
A	4 1/2"	1 1/2"
B	5 1/8"	1 1/2"
C	5 1/8"	1 1/2"
D	4 1/2"	3/8"

Figure 2-5: Test Specimen Dimensions

2.2 SPECIMEN DESIGN

The specimens were designed to fail at the stiffener detail location. If not designed properly, failure could occur elsewhere along the specimen such as at the end of the web plate simulation as shown in Figure 2-6.

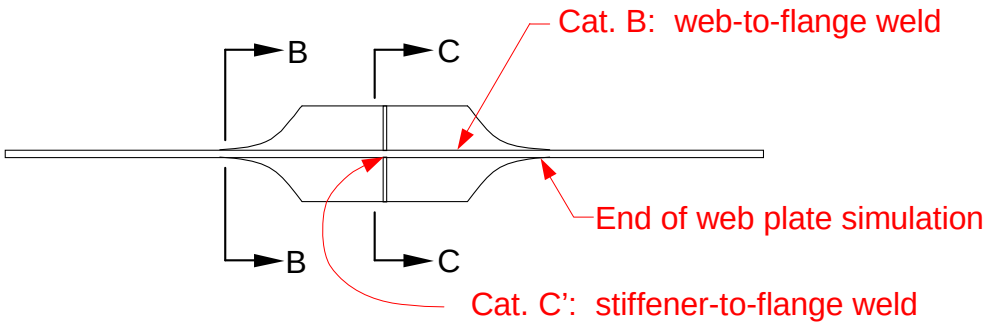

Figure 2-6: Location of Fatigue Categories

The AASHTO bridge specification was used to identify the fatigue resistance categories associated with the specimen. These categories help determine the fatigue life of a given detail as a function of plate geometry and orientation with respect to the direction of loading. Figure 2-6 identifies the locations on the specimen that were considered for fatigue resistance classification. For design calculations, the stiffener-to-flange weldement was determined to be a category C' fatigue detail. The end of the web-to-flange weldement was considered to be a category B fatigue detail along its length.

Figure 2-7 shows the nominal fatigue resistance of category B details and category C' details. Figure 2-7 shows that category C' details are more severe than category B details. At any given nominal stress range, S_R, a category C' detail will fail at less cycles before a category B detail. Therefore, geometry and plate sizing of the specimen was selected such that the category C' stiffener detail governed the design fatigue life. Threshold curves in Figure 2-7 indicate infinite fatigue life at a stress range below the dashed lines.

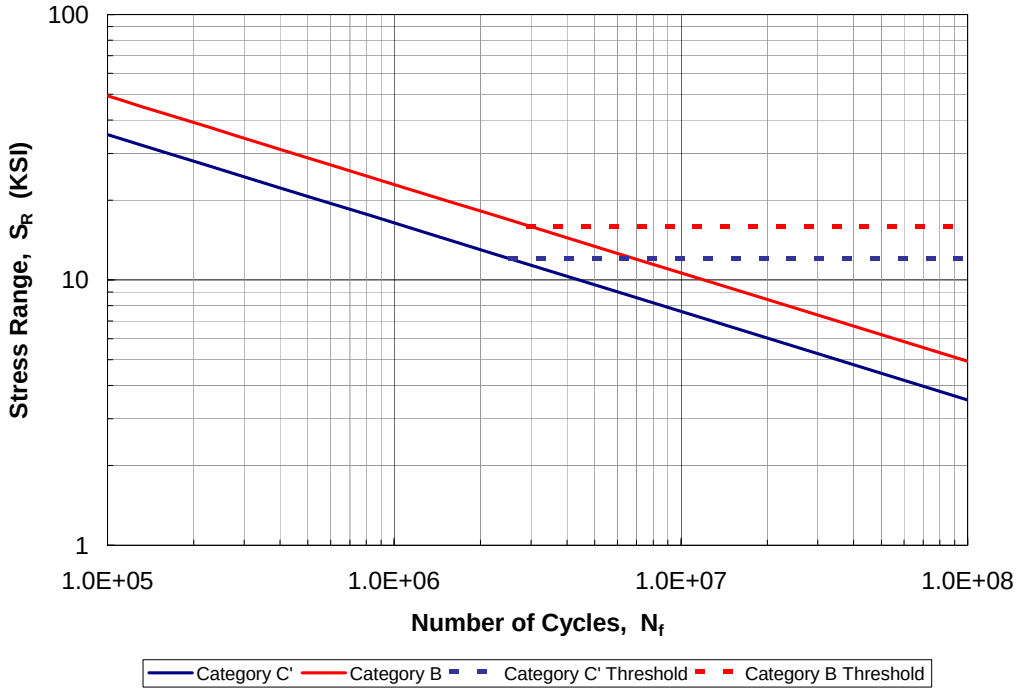

Figure 2-7: AASHTO Nominal Fatigue Resistance Categories B & C'

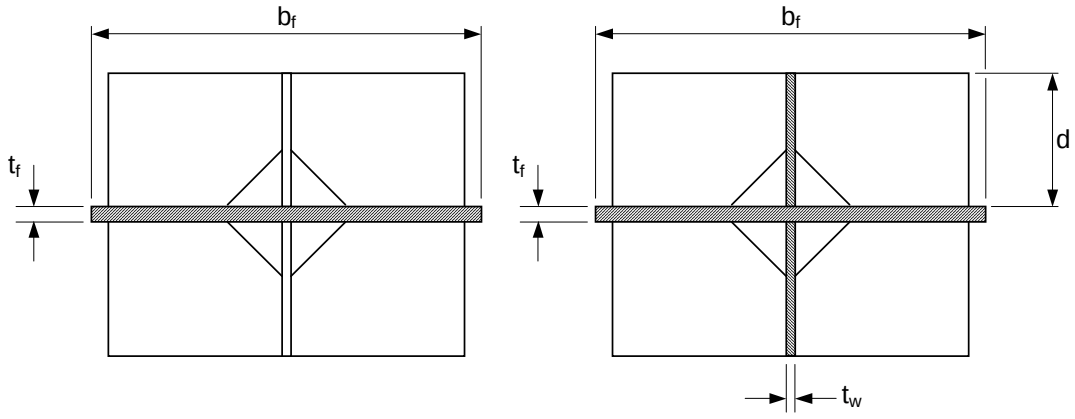

Section B-B

$$\text{Area} = t_f \times b_f$$

Section C-C

$$\text{Area} = 2 \times (t_w \cdot d) + (t_f \cdot b_f)$$

Figure 2-8: Area Used For Calculating Nominal Stress

All specimens were tested under cyclic loading at a nominal stress range, S_R, of 20 ksi (138 MPa) at section C-C shown in Figures 2-6 and 2-8. The stress range is the difference between the minimum and maximum nominal stresses. The minimum and maximum nominal stresses across section C-C were 5 ksi (34.5 MPa) and 25 ksi (172 MPa), respectively. These nominal stresses were calculated by dividing the applied axial load on the specimen by the area of the web and flange plates shown in Figure 2-8, Section C-C. The lower stress limit corresponded to an axial load of 35 kips (156 kN), whereas the upper stress limit was produced by an axial load of 175 kips (778 kN). It should be noted that the stress range at section B-B shown in Figures 2-6 and 2-8 is higher than the stress range at section C-C due to the decrease in area. The stress range at section B-B is 26.7 ksi (184 MPa).

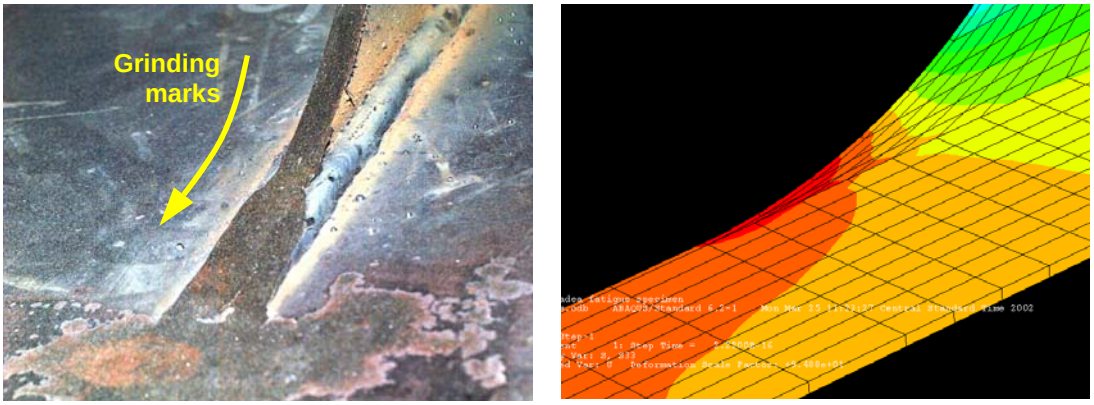

Figure 2-9: Radial Transition Region Showing High Stress

The radial taper shown in Figure 2-9 was used at the end of the simulated web plate simulation to minimize the chance of fatigue failure. Transition from the simulated web to the flange plate resulted in a decrease in cross-sectional area, and thus an increase in the stress range from 20 ksi to 26.7 ksi. Figure 2-8

illustrates this difference between these cross-sectional areas. Additionally, a finite element model discussed in the following section shows that high principal stresses exist at the radial taper in Figure 2-9. The radial taper created a high stress concentration at the end of the web. Defined as the maximum principal stress divided by the nominal stress, the stress concentration factor at the end of the taper was approximately 1.2. The transition region was grinded flush to the flange plate using a disk grinder and belt sander to minimize the increase in stress and to eliminate any discontinuities from the welds. Thus, the fatigue performance of the taper transition was estimated as a category B detail. The required flange and web sizes were determined based on the nominal fatigue resistance of the stiffener-to-flange connection in comparison to the web-to-flange weldement. The final plate sizing satisfies the fatigue resistance demands such that specimen failure is constrained to the stiffener-to-flange connection.

The specimen was designed to make the stiffener-to-flange weld control the fatigue life of the specimen. The ratio of area B-B to area C-C (refer to Figure 2-8) was determined to prevent a fatigue failure at the radiussed end of the web-to-flange weld.

The test specimen design calculations that produce the desired failure are now presented. The predicted fatigue life of the stiffener-to-flange detail is 550,000 cycles at a nominal stress range of 20 ksi (138 MPa). The predicted fatigue life of the web-to-flange weld toe at the end of the web simulation (refer to Figure 2-6) is 632,575 cycles at a nominal stress range of 26.7 ksi (184 MPa). All stresses were kept within the capacity of the actuator and test frame to be discussed in Chapter 3 of this report.

Nomenclature :

b_f = flange width, in.

t_f = flange thickness, in.

d = stiffener height, in.

t_w = web thickness, in.

N = cycles to failure

A = detail category constant

S_R = stress range, ksi

P_R = load range, kips

From AASHTO bridge specification detail category constants for B and C are

$$A_B = 120 \times 10^8$$

$$A_C = 44 \times 10^8$$

The fatigue life is calculated as follows,

$$N = AS_R^{-3}$$

So,

$$N_B = \left(120 \times 10^8\right) \cdot \left(S_{RB}^{-3}\right)$$

$$N_C = \left(44 \times 10^8\right) \cdot \left(S_{RC}^{-3}\right)$$

The fatigue life at the end of the web - to - flange weld, category B, must be greater than the fatigue life at the stiffener, category C'

$$N_B > N_C$$

$$\left(120 \times 10^8\right) \cdot \left(S_{RB}^{-3}\right) > \left(44 \times 10^8\right) \cdot \left(S_{RC}^{-3}\right)$$

therefore,

$$\frac{S_{RC}}{S_{RB}} > 0.716 \qquad \text{or} \qquad S_{RB} < 1.40 \cdot S_{RC}$$

The areas shown in Figure 2 - 8 are used to express the stress range at the respective category sections as :

$$S_{RB} = \frac{P_R}{b_f \cdot \left(t_f\right)} \qquad S_{RC} = \frac{P_R}{b_f \cdot \left(t_f\right) + 2 \cdot \left(t_w\right) \cdot d}$$

The required stress range is 20 ksi at Section C - C. The upper and lower limit stresses are 25 ksi and 5 ksi, respectively. The maximum stress must require a load that does not exceed the 220 kip capacity of the actuator.

Thus,

$$S_{RC} = \frac{P_R}{b_f \cdot (t_f) + 2 \cdot (t_w) \cdot d} = 20 \text{ ksi}$$

Or,

$$S_{maxC} = \frac{P_{max}}{b_f \cdot (t_f) + 2 \cdot (t_w) \cdot d} = 25 \text{ ksi}$$

$$25 \cdot \left[(b_f \cdot t_f) + (2 \cdot t_w \cdot d) \right] = P_{max}$$

$$25 \cdot \left[(b_f \cdot t_f) + (2 \cdot t_w \cdot d) \right] \leq 220 \text{ kips}$$

*T*he dimensions shown below satisfie the design constraints :

$b_f = 10.5$ in.

$t_f = 0.5$ in.

$d = 3.5$ in.

$t_w = 0.25$ in.

Which provide the areas :

Area at CC $= 7$ in.^{2}

Area at BB $= 5.25$ in.^{2}

The corresponding loads are :

$P_{max} = 175$ kips $\quad P_{min} = 35$ kips $\quad P_R = 140$ kips

The nominal stresses at each section are :

$S_{maxC} = 25$ ksi $\quad S_{minC} = 5$ ksi $\quad S_{RC} = 20$ ksi

$S_{maxB} = 33.3$ ksi $\quad S_{minB} = 6.67$ ksi $\quad S_{RB} = 26.7$ ksi

The design constraints are satisfied as :

$P_{max} = 175 \text{ kips} < 220 \text{ kips}$ O.K.

$S_{RB} = 26.7 \text{ ksi} < 1.40 \cdot S_{RC} = 28 \text{ ksi}$ O.K.

2.2.1 Finite Element Model

A linear-elastic finite element model was developed to determine whether or not the full cross-sectional area at the stiffener-to-flange connection was being developed as assumed in the design calculations. The model was used to investigate the development of stress in the web and flange sections in order to report more accurately the actual stress range adjacent to the stiffener connection.

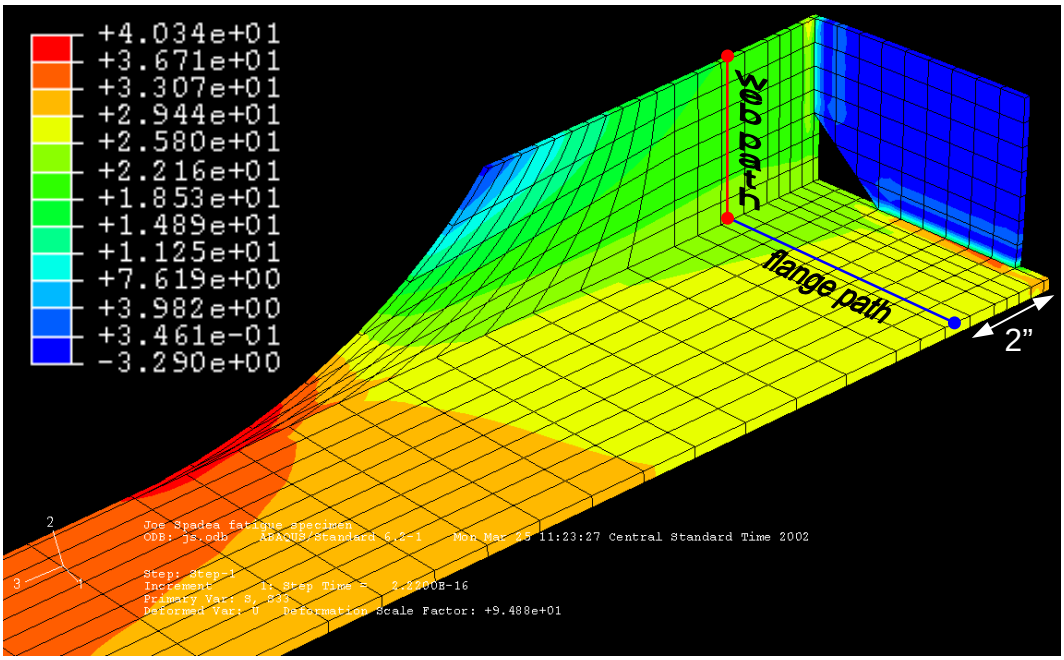

Figure 2-10: Finite Element Principal Stress Results (ksi)

One-eighth (1/8) of the specimen was modeled in Abaqus using symmetry boundary conditions and a modulus of elasticity of 29,600 ksi (20.4×10^4 MPa). Three-dimensional continuum brick elements were used to model the specimen. Brick elements C3D15 were used for the web and stiffener. Brick elements C3D20 were used for the flange. The C3D15 elements have 15 nodes and the C3D20 elements have 20 nodes. Both elements use full integration and quadratic interpolation. The mesh size varied depending on the flange, web, and stiffener

components being modeled. A small mesh of 0.25 in. long by 0.5 in. wide (6.35 mm by 12.7 mm) elements was used for the flange and web near the stiffener over a length of approximately 1.0 in. (25.4 mm). The length of the flange and web elements increased further away from the stiffener in the longitudinal direction, and the width remained constant perpendicular to the direction of loading. The flange and web element thickness were 0.25 in. (6.35 mm) and 0.125 in. (3.2 mm), respectively. 0.5 in. long by 0.5 in. wide by 0.125 in. thick (12.7 mm by 12.7 mm by 3.2 mm) elements were used for the stiffener.

Figure 2-10 shows the results of the finite element analysis. Recall that the nominal upper limit stress at the stiffener-to-flange connection is 25 ksi (172 MPa). The stresses shown in Figure 2-10 caused by the maximum static load of 175 kips (778 kN) were generated in Abaqus by applying a uniformly distributed tensile load at the plate end (gripped portion of specimen). The analysis shows that the stress in the flange plate was higher than the stress in the web plate.

A flange path and a web path are shown in Figure 2-10. The paths are located at the same distance from the stiffener as strain gages discussed in Chapter 3.3.2.2. It should be noted that a higher value of stress exists immediately adjacent to the stiffener-to-flange weld toe as shown in Figure 2-10. This stress is approximately 33 ksi (228 MPa) at maximum applied load, and this stress increase is due to the abrupt change in geometry caused by the stiffener detail.

Figure 2-11 shows a plot of principal stress along the flange surface corresponding to the “flange path” labeled in Figure 2-10. A maximum stress of approximately 27.3 ksi (188 MPa) occurs near the edge of the flange. A minimum stress of 23.8 ksi (164 MPa) occurs at the web connection. The average upper limit stress in the flange is 26.2 ksi (181 MPa).

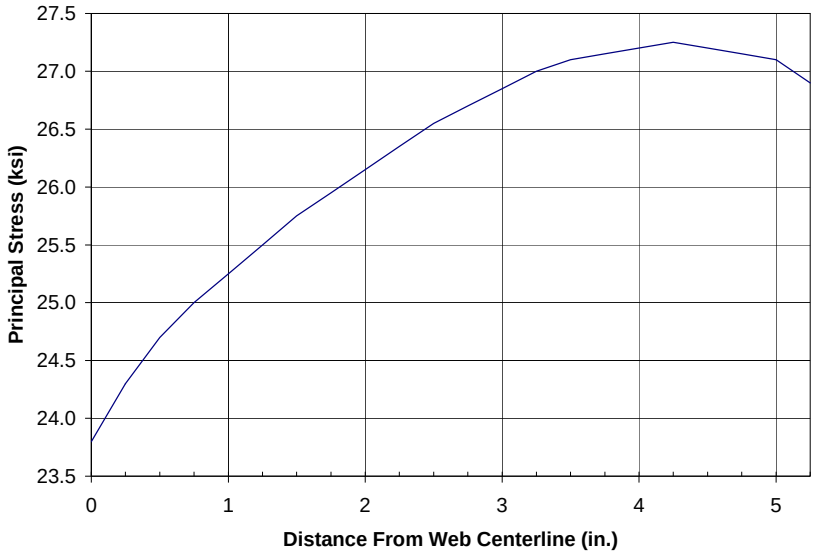

Figure 2-11: Principal Stress Along Flange Path

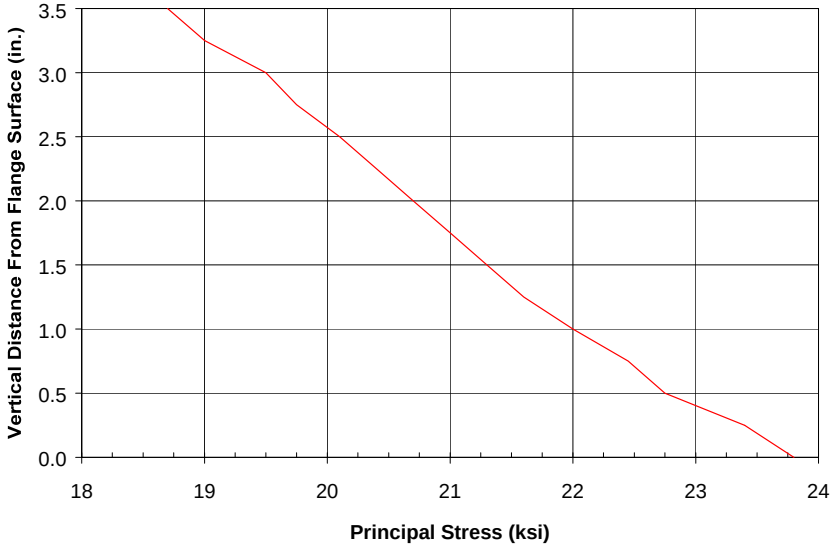

Figure 2-12: Principal Stress Along Web Path

Figure 2-12 shows a plot of principal stress along the web centerline corresponding to the "web path" depicted in Figure 2-10. The maximum stress of approximately 23.8 ksi (164 MPa) occurs at the flange connection. A minimum stress of approximately 18.7 ksi (129 MPa) occurs at the top of the web plate. The average upper limit stress in the web is 21.1 ksi (145 MPa).

The results of the finite element model showed that the stress was not uniform near the stiffener section. In particular, stress in the web was not fully developed. The largest web stress was less than the nominal upper limit stress of 25 ksi (172 MPa). Stress in the flange edge was higher than the stress at the flange centerline. Stresses reported in the flange will directly influence the fatigue life of the stiffener-to-flange connection. The larger stress at the flange edge will reduce the fatigue life at the flange edge.

The average principal stress in the flange under the 175 kip maximum loading condition was determined to be 26.2 ksi (181 MPa). Under the 35 kip minimal loading condition, the principal stress is [$^{35}/_{175}$] x 26.2 ksi, or 5.24 ksi (36.1 MPa) with a resulting stress range of 21 ksi (145 MPa) in the flange.

2.3 SPECIMEN FABRICATION

The materials and welding procedure used to fabricate the test specimens are discussed in this section. The materials and welding process reflect those used by TxDOT manufacturers of steel plate girders. Figure 2-13 shows a specimen being welded by a certified welder at Ferguson Structural Engineering Laboratory.

Figure 2-13: Welding the Web to the Flange

2.3.1 Materials and Welding Parameters

A572 Gr 50 steel was used in the fabrication of all test specimens. 10.5 in. by 0.5 in. (267 mm by 13 mm) steel plate and 3.5 in. by 0.25 in. (89 mm by 6.35 mm) bar stock were used for all specimens. A572 Gr 50 steel has a minimum yield stress of 50 ksi (345 MPa) and an assumed modulus of elasticity of 29000 ksi ($2x10^5$ MPa).

Gas metal arc welding (GMAW) was used to weld the specimens. All welds were nominal 0.25 in. fillet welds (6.35 mm). 0.045 in. diameter (1.14

mm) FabCOR 86R E70C-6M metal-cored electrode wire was used with a travel speed of approximately 16 IPM and a wire speed of 310 IPM. The machine was set to 200 amps at 26 volts. The shielding gas was a mixture of 90% Argon and 10% CO_2.

2.3.2 Assembly

Figure 2-14 shows several A572 Gr 50 steel flange, web, and stiffener parts used for the specimens prior to welding. Stiffener and flange undercuts were intentionally created during the welding process to produce worst-case scenarios.

Figure 2-14: Steel Parts Prior to Welding

The 0.5 in. thick (13mm) flange used for the specimen was cut from 120 in. by 10.5 in. (3048 mm by 267 mm) plates using a band saw. The 0.25 in. thick (6.4 mm) web and stiffener parts were cut from 240 in. by 3.5 in. (6096 mm by 89 mm) bar stock using a band saw. The web section radius was then cut using a plasma torch.

Figure 2-15: Weld Start-Stop Repair

The welding sequence varied throughout the project relative to each specimen type. This variation was due to the efforts to eliminate defects that occurred at weld starts and stops. Figure 2-15 shows a photo of a start-stop that was repaired by grinding and rewelding the web-to-flange weld.

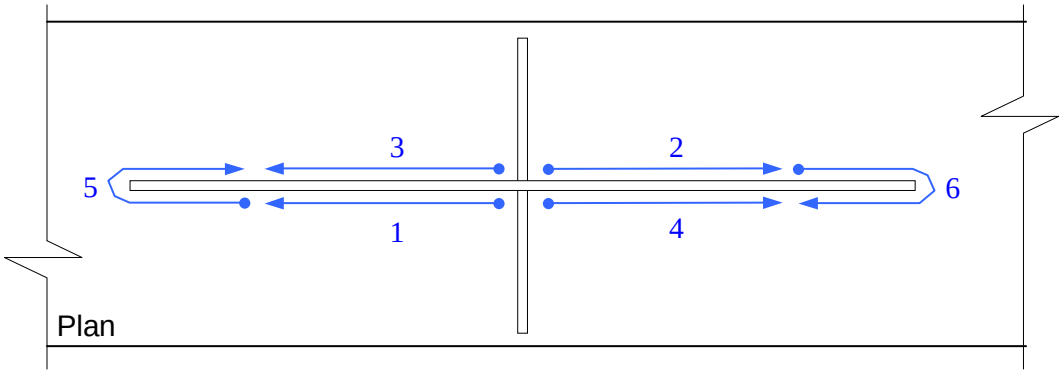

Figure 2-16: Welding Sequence for Specimens 1A, 2A, 3A, and 7C

Specimens 1A, 2A, 3A, and 7C were welded using the same sequence. The web and the stiffeners were tacked to one side of the flange plate. This was

next repeated on the opposite side. Welds were then made in the horizontal position in the sequence illustrated in Figure 2-16. The stiffeners were next welded to the flange in the horizontal position starting from the interior clip, continued around the stiffener edge, and back to the clip. In some cases, the weld was stopped midway between the stiffener edge and clip. A short pass was then used to complete the weld seal. This was done on both stiffeners on the top surface of the flange and then repeated on the opposite surface. The stiffeners were then welded to the web in the horizontal position.

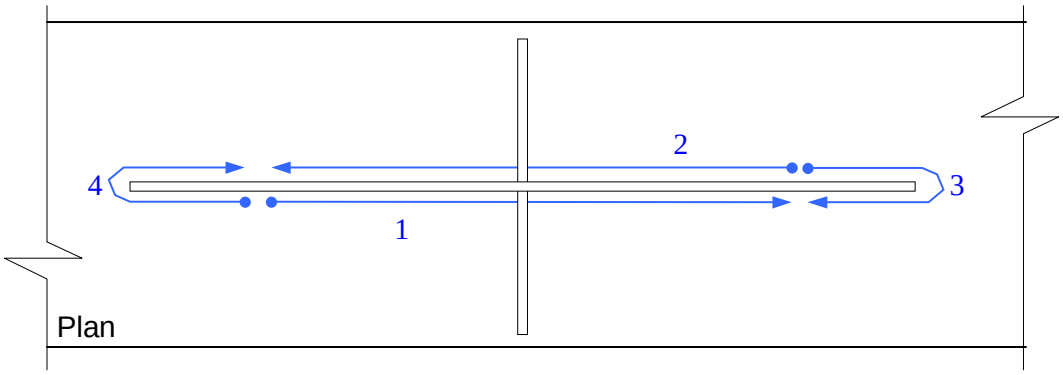

Figure 2-17: Welding Sequence for Specimens 4B- 6B, and 10D-12D

Specimens 4B, 5B, 6B, 10D, 11D, and 12D were welded using a modified sequence shown in Figure 2-17. First, the web was welded to the flange in the horizontal position using the sequence shown in Figure 2-17. Next, the stiffeners were tacked to the same side. This process was repeated on the opposite side. The stiffeners were next welded to the flange in the overhead position. The overhead position was used to produce severe flange undercuts at the edge of the stiffeners. Lastly, the stiffeners were welded to the web in the horizontal position. Weld start and stops on specimens 4B, 5B, and 6B were remelted using a TIG torch. Weld start and stops on specimens 10D, 11D, and 12D were removed by grinding and rewelded.

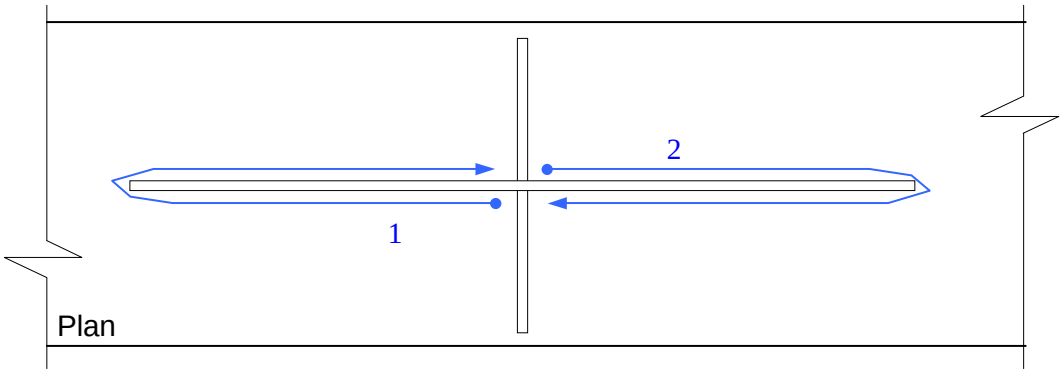

Figure 2-18: Welding Sequence for Specimens 8C and 9C

Specimens 8C and 9C were welded using a third sequence. The web and the stiffeners were tacked to one side of the flange plate. This was next repeated on the opposite side. The web-to-flange welds were then made in the horizontal position as illustrated in Figure 2-18. The continuous welds eliminated the chance of premature fracture due to weld start and stop defects. The stiffeners were next welded to the flange in the overhead position and then to the web in the horizontal position. The overhead position was used to produce worst-case flange undercuts. AASHTO D1.5-95 Bridge Welding Code guidelines were employed for the removal of the edge defects for type C specimens. The undercut was removed by grinding into the base metal with a finished surface slope not greater than one in ten in the direction of loading. Grinding marks were finished parallel to the direction of loading.

After the assembly was completed, the radial transition sections were ground smooth at the ends using a disk grinder. The surface grinding marks were finished parallel with the direction of loading using a belt sander. This was done to reduce the risk of premature fracture caused by perpendicular grinding marks.

2.4 DETAILS OF WELD UNDERCUTS

Undercuts were intentionally produced during the fabrication of the type A, B, C, and D specimens. Attempts were made to create the largest undercut possible to produce worst-case scenarios. Undercut locations and characteristics are discussed in this section for all specimens.

Type A specimens were used to investigate the influence of undercutting on the fatigue performance caused by wrapping the stiffener weld around the interior clip and exterior edges of the stiffener. A close-up of the type A stiffener detail is shown in Figure 2-19. Arrows are used in the figure to indicate the points of undercutting.

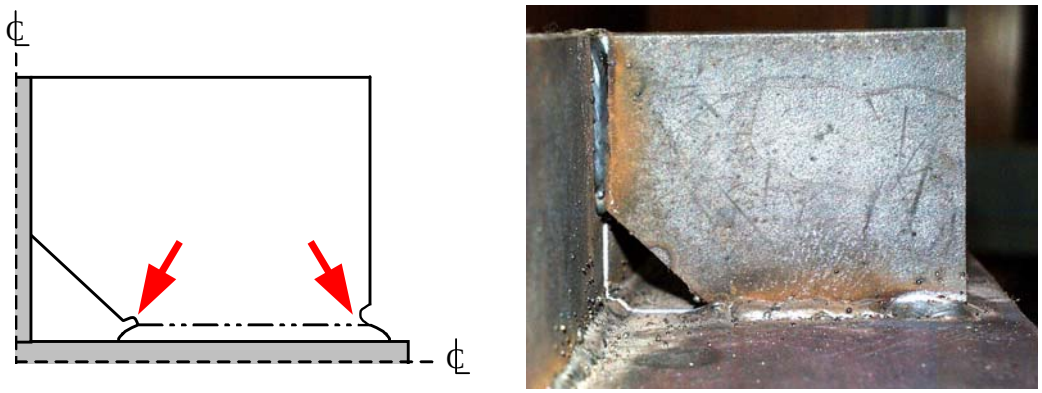

Figure 2-19: Location of Undercut for Specimen Type A

Interior stiffener undercuts varied in size and shape. Some undercuts were large and circular as pictured in Figure 2-20. Other undercuts were small, narrow, or invisible to inspection as shown in Figure 2-21. Minimal to no undercutting occurred at the exterior edge of the stiffener as shown in Figure 2-22.

Specimen 2A - Left Stiffener

Specimen 2A – Right Stiffener

Figure 2-20: Large Circular Interior Stiffener Undercuts

Specimen 1A – Left Stiffener

Specimen 1A Right Stiffener

Figure 2-21: Minimum Interior Stiffener Undercuts

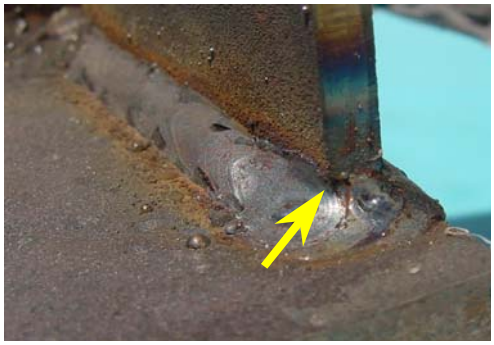

Figure 2-22: Specimen A Stiffener Undercut

The Type B stiffener detail is shown in Figure 2-23. Type B specimens were used to observe undercutting effects at both the interior clip weld wrap and the exterior stiffener-to-flange weld wrap. Because the stiffener is extended to the edge of the flange, undercutting of the flange plate at the exterior edge also occurred. Wrapping the weld around the exterior edge also causes minimal undercutting of the stiffener as shown in Figure 2-24.

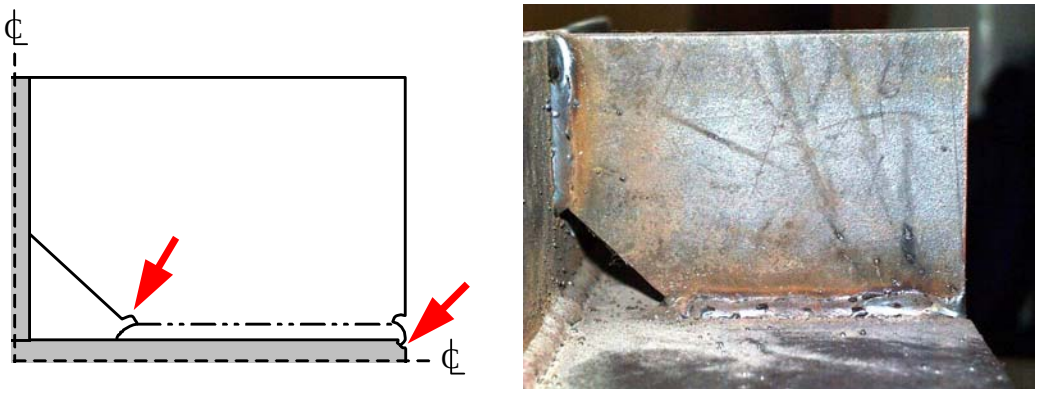

Figure 2-23: Location of Undercut for Specimen Type B

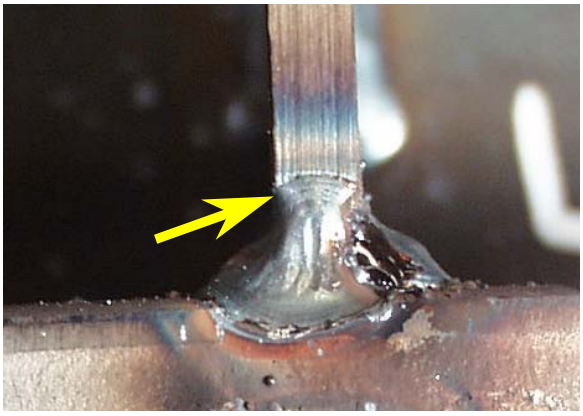

Figure 2-24: Specimen B Stiffener Undercut

Flange undercuts occurred as the stiffener weld was wrapped around the exterior edge of the stiffener. The flange undercuts were shaped like an hourglass

and were consistent among specimens. Figure 2-25 shows photographs of the flange undercuts.

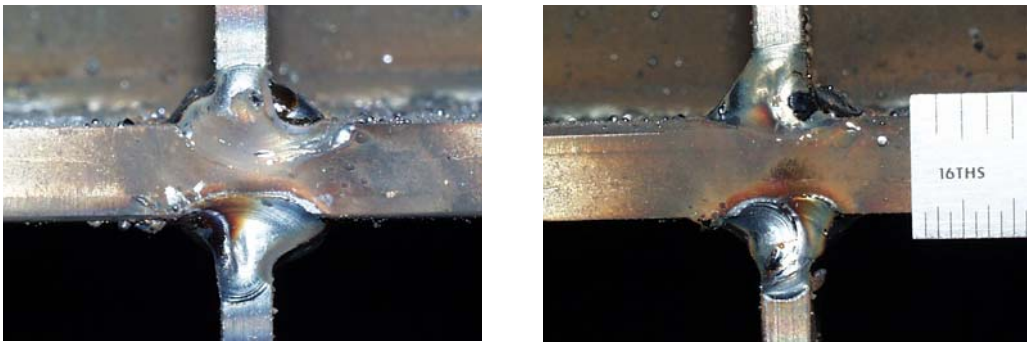

Figure 2-25: Specimen B Flange Undercuts

Type C specimens are identical to type B specimens with the flange edge undercut removed by grinding after welding. The type C stiffener detail is shown in Figure 2-26. The photograph in Figure 2-26 shows the depth of grinding into the flange needed to remove the flange undercut.

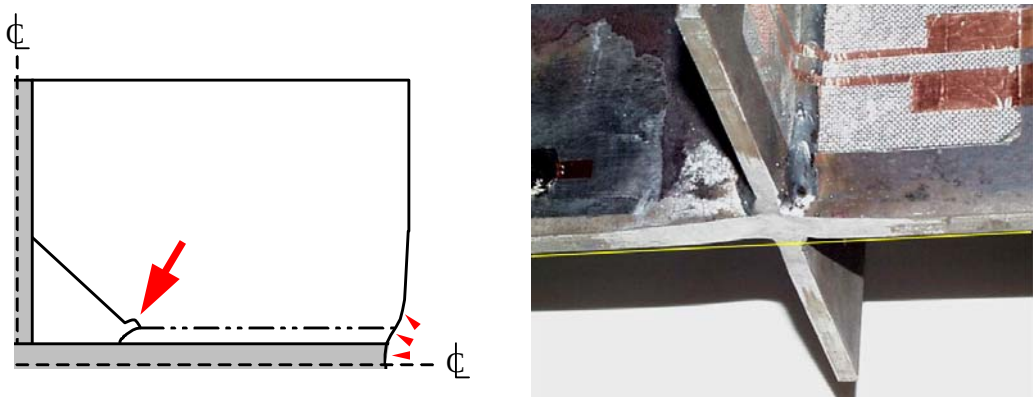

Figure 2-26: Location of Undercut for Specimen Type C

AASHTO AWS D1.5-95 Bridge Welding Code guidelines (section 3.2) were employed for the removal of the edge undercuts. The AWS procedure and requirements are identical to the TxDOT fracture critical defect repair procedures. The undercut was removed by grinding past the maximum undercut depth with a

finished surface slope not greater than one in ten in the direction of loading. Grinding marks were finished parallel to the direction of loading as pictured in Figure 2-27.

Figure 2-27: Before and After Flange Grinding

Type D specimens were used to investigate the impact on the fatigue life caused by minimizing the clip size and completely welding this area closed. The clip size was reduced to 0.375 in. (10 mm) and welds were overlapped to completely eliminate the opening as shown in Figure 2-28. Similar to the type A specimens, minimal to no undercutting occurred at the exterior edge of the stiffener in the type D specimens.

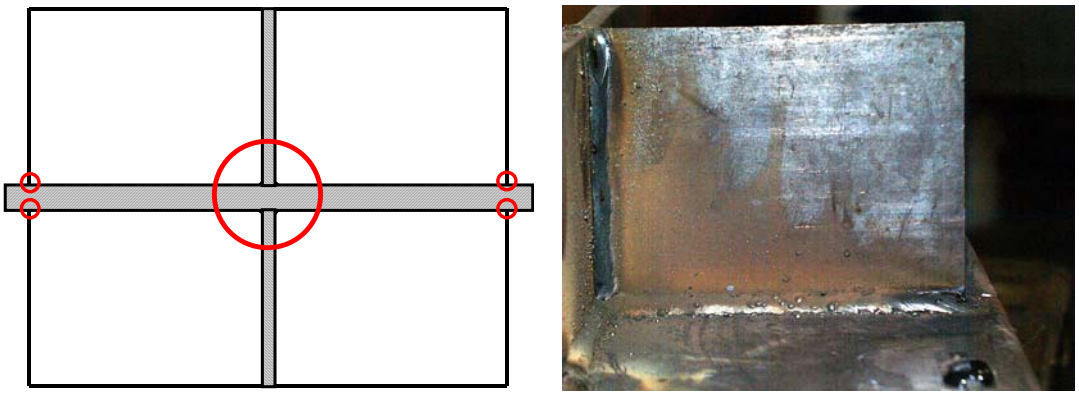

Figure 2-28: Specimen Type D Showing No Clip

2.5 MEASURING OF UNDERCUTS

The sizes of the undercuts are presented in this section. Undercuts were measured with calipers and the values are presented in this section. The undercuts were measured with calipers to an accuracy of ±0.005 inches. The length, width, and depth into the thickness of the stiffener were measured for the interior and exterior stiffener undercuts. The length, width, and depth into the thickness of the flange were measured for the flange undercuts.

2.5.1 Type A Specimen Undercuts

Undercut locations were labeled based on their orientation with respect to their location in the test frame. Figure 2-29 shows the location and nomenclature used for classification of type A specimen undercuts. The interior and exterior stiffener undercuts were located on the top half (T) or bottom half (B) of the specimen midsection.

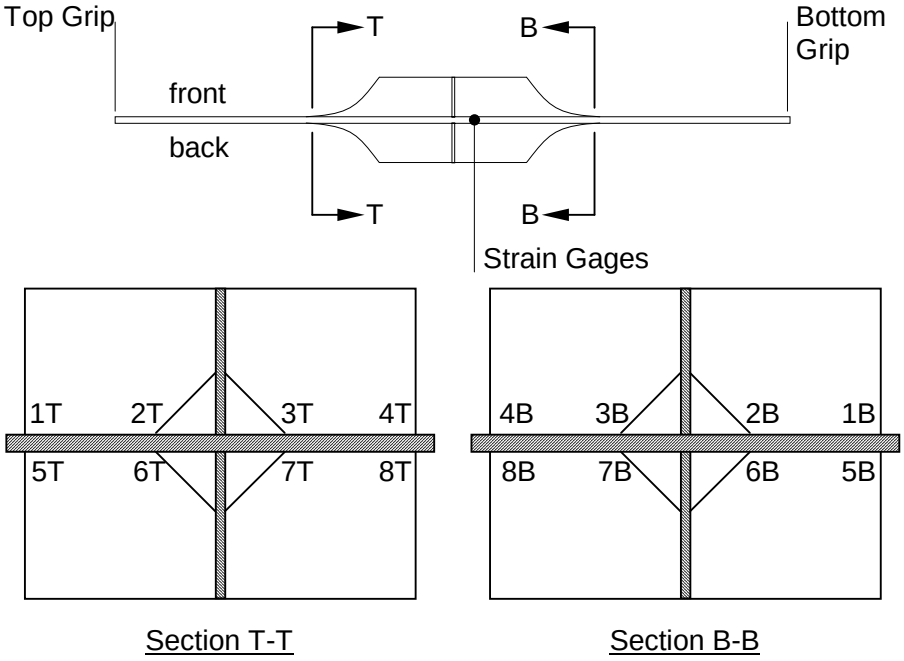

Figure 2-29: Specimen A Undercut Identification

Table 2-1 lists the stiffener undercut dimensions corresponding to the locations in Figure 2-29. Figure 3-30 illustrates the dimensions that were recorded for the specimen A stiffener undercuts. Depth, d, refers to the depth into the stiffener thickness. Measurements are given in inches.

Table 2-1: Specimen A Stiffener Undercut Measurements (inches)

Undercut	1A			2A			3A		
I.D.	L	h	d	L	h	d	L	h	d
1T	0	0	0	0	0	0	0.050	0.050	0.050
1B	0.350	0.350	0.035	0.180	0.320	0.120	0	0	0
2T	0.050	0.050	0.050	0.392	0.263	0.125	0	0	0
2B	0	0	0	0.102	0.100	0.125	0.075	0.050	0.070
3T	0.244	0.100	0.125	0.316	0.092	0.125	0.075	0.050	0.050
3B	0	0	0	0.113	0.145	0.125	0.050	0.050	0.050
4T	0.090	0.150	0.113	0	0	0.0	0.075	0.075	0.075
4B	0	0	0	0	0	0.0	0.075	0.075	0.075
5T	0.035	0.079	0.065	0.050	0.050	0.050	0.075	0.100	0.075
5B	0	0	0	0.075	0.075	0.075	0.050	0.050	0.050
6T	0.080	0.085	0.080	0.050	0.050	0.050	0	0	0
6B	0.085	0.15	0.100	0.239	0.184	0.125	0	0	0
7T	0	0	0	0.162	0.086	0.125	0	0	0
7B	0	0	0	0.209	0.150	0.125	0	0	0
8T	0	0	0	0.050	0.050	0.050	0.100	0.100	0.100
8B	0	0	0	0.050	0.050	0.050	0.100	0.100	0.100
Avg.	0.058	0.060	0.036	0.124	0.101	0.079	0.045	0.044	0.043
Max.	0.350	0.350	0.125	0.392	0.320	0.125	0.100	0.100	0.100

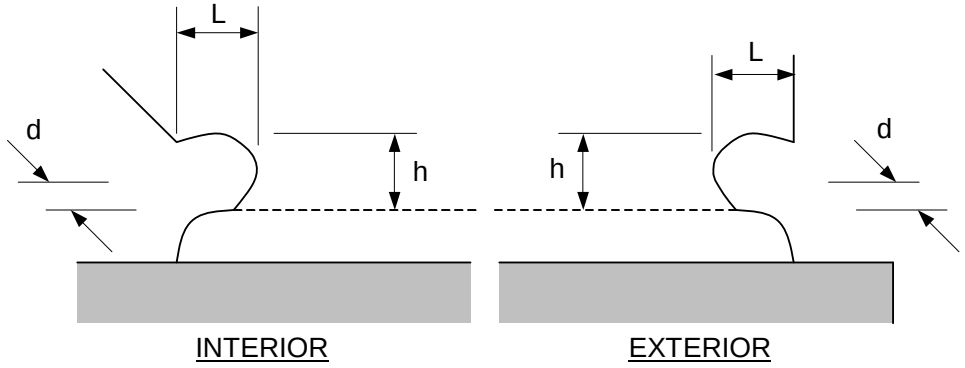

Figure 2-30: Specimen A Stiffener Undercut Dimensions

Table 2-1 shows that specimen 2A consistently had larger undercuts than specimens 1A and 3A. Specimen 2A had the most undercuts of the three specimens. Specimen 3A had the smallest measured undercuts.

2.5.2 Type B Specimen Undercuts

Figure 2-31 shows the location and nomenclature used for classification of type B specimen undercuts. The flange undercuts (E) are located on the free edge of the flange plate at the stiffener location.

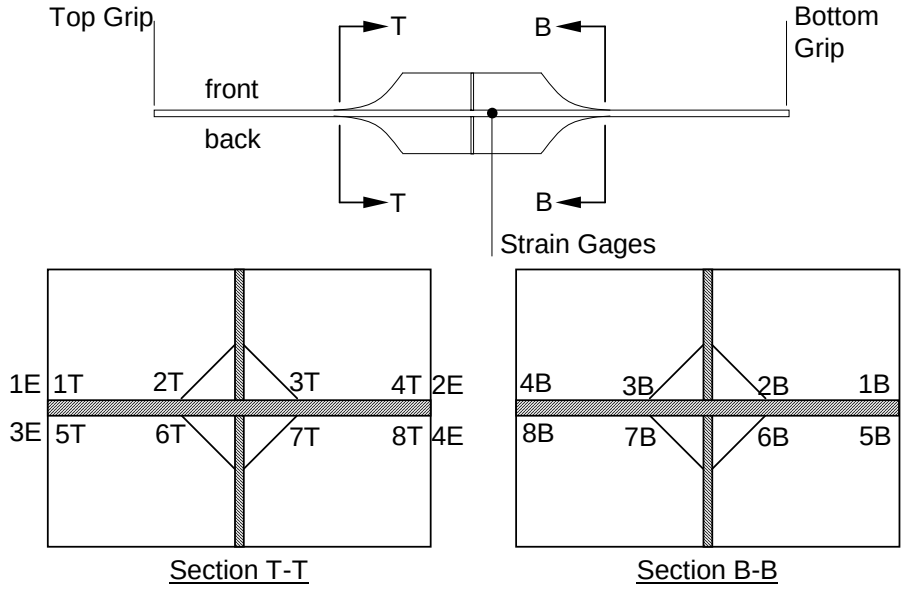

Figure 2-31: Specimen B Undercut Identification

Table 2-2 lists the stiffener undercut dimensions corresponding to the locations in Figure 2-31. It should be noted that small undercutting occurred at the exterior stiffener locations 1, 4, 5, and 8. The stiffener undercut sizes were consistent among the three specimens. The average length of the undercuts was approximately 0.16 in. (4 mm), and the average height was .052 in (1.3 mm). The average depth was 0.044 in. (1 mm).

Table 2-2: Specimen B Stiffener Undercut Measurements (inches)

Undercut	4B			5B			6B		
I.D.	L	h	d	L	h	d	L	h	d
1T	0.050	0.050	0.050	0.050	0.100	0.050	0	0	0
1B	0.050	0.100	0.070	0.050	0.070	0.050	0	0	0
2T	0	0	0	0	0	0	0.050	0.050	0.050
2B	0.050	0.050	0.050	0.186	0.125	0.125	0.050	0.050	0.050
3T	0.050	0.050	0.050	0.200	0.065	0.125	0.050	0.050	0.050
3B	0	0	0	0.050	0.050	0.050	0.115	0.050	0.100
4T	0.064	0.085	0.050	0	0	0	0	0	0
4B	0.050	0.115	0.100	0.070	0.170	0.075	0.120	0.100	0.070
5T	0.050	0.080	0.100	0	0	0	0.050	0.100	0.050
5B	0.050	0.120	0.050	0	0	0	0.060	0.060	0.050
6T	0.100	0.050	0.050	0.050	0.050	0.050	0.050	0.050	0.050
6B	0	0	0	0.050	0.050	0.050	0.064	0.088	0.090
7T	0	0	0	0.050	0.050	0.050	0	0	0
7B	0.135	0.105	0.070	0.360	0.110	0.050	0.0	0.0	0
8T	0.060	0.120	0.125	0.050	0.050	0.050	0.050	0.050	0.050
8B	0	0	0	0	0	0	0	0	0
Avg.	0.044	0.058	0.048	0.073	0.056	0.045	0.041	0.041	0.038
Max.	0.135	0.120	0.125	0.360	0.170	0.125	0.120	0.100	0.100

Table 2-3 lists the flange undercut dimensions corresponding to the “E” locations in Figure 2-31. Figure 3-33 illustrates the dimensions that were measured for the specimen B flange undercuts. It should be noted that the flange undercuts were considered more detrimental to the fatigue life of the specimen than the exterior stiffener undercuts because of their direct orientation to loading. Average measured values were consistent among all three specimens. The average length of the flange undercuts was approximately 0.5 in. (13 mm), and the average depth was over 0.125 in. (3 mm). The average width of the flange undercuts was 0.072 in. (2 mm).

Table 2-3: Specimen B Flange Undercut Measurements (inches)

Undercut	4B			5B			6B		
I.D.	L	d	w	L	d	w	L	d	w
1E	0.680	0.100	0.050	0.400	0.150	0.050	0.610	0.200	0.050
2E	0.725	0.125	0.050	0.570	0.175	0.070	0.468	0.100	0.100
3E	0.514	0.114	0.074	0.520	0.110	0.075	0.486	0.090	0.060
4E	0.460	0.145	0.110	0.554	0.125	0.050	0.690	0.110	0.125
Avg.	0.595	0.121	0.071	0.511	0.140	0.061	0.564	0.125	0.084
Max.	0.725	0.145	0.110	0.570	0.175	0.075	0.690	0.200	0.125

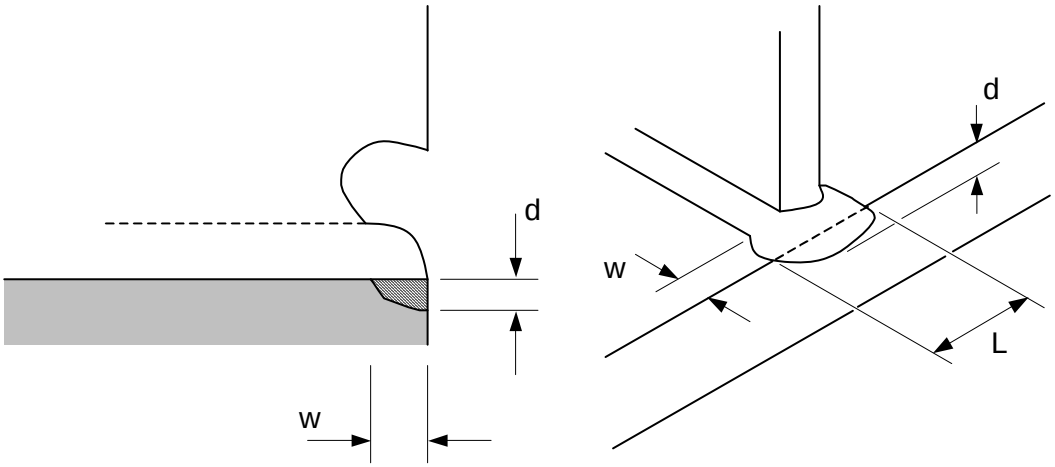

Figure 2-32: Specimen B Flange Undercut Dimensions

2.5.3 Type C Specimen Undercuts

Type C specimen undercuts were recorded in the same fashion as the type B specimen undercuts. After recording the flange undercuts, a disk grinder was used to remove the undercut from the flange according to the AASHTO D1.5-95 Bridge Welding Code guidelines.

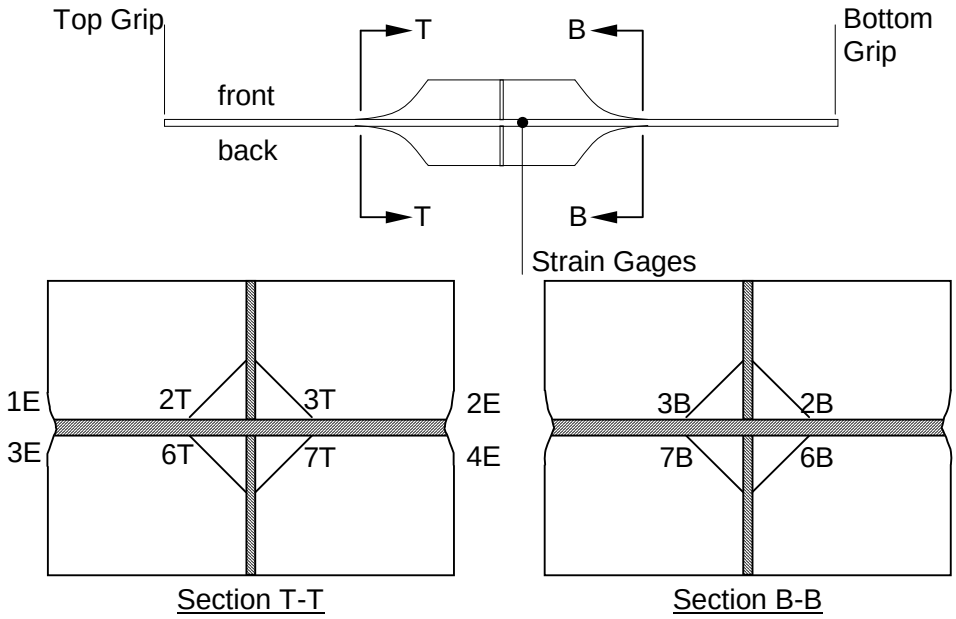

Figure 2-33: Specimen C Undercut Identification

Table 2-4 lists the interior stiffener undercut dimensions corresponding to the locations in Figure 2-33. It should be noted that the undercuts at the exterior stiffener edge were removed during grinding of the flange undercut. Therefore, only interior stiffener undercuts were listed. The flange undercuts were recorded prior to removal by grinding. These values are given in Table 2-5, and the dimensions are illustrated in Figure 2-32.

Table 2-4: Specimen C Stiffener Undercut Measurements (inches)

Undercut	7C			8C			9C		
I.D.	L	h	d	L	h	d	L	h	d
2T	0	0	0	0	0	0	0	0	0
2B	0	0	0	0	0	0	0.050	0.050	0.050
3T	0	0	0	0.050	0.050	0.050	0.130	0.070	0.125
3B	0.050	0.050	0.050	0.060	0.080	0.050	0	0	0
6T	0	0	0	0	0	0	0.050	0.050	0.050
6B	0	0	0	0.080	0.050	0.125	0.135	0.075	0.100
7T	0.120	0.060	0.060	0.200	0.100	0.120	0	0	0
7B	0.065	0.060	0.100	0	0	0	0	0	0
Avg.	0.029	0.021	0.026	0.049	0.035	0.043	0.046	0.031	0.041
Max.	0.120	0.060	0.100	0.200	0.100	0.125	0.135	0.075	0.125

Table 2-5: Specimen C Flange Undercut Measurements (inches)

Undercut	7C			8C			9C		
I.D.	L	d	w	L	d	w	L	d	w
1E	0.500	0.063	0.125	0.625	0.156	0.063	0.688	0.188	0.125
2E	0.875	0.250	0.125	0.500	0.125	0.125	0.625	0.125	0.031
3E	0.625	0.125	0.063	0.563	0.188	0.063	0.688	0.063	0.250
4E	0.750	0.125	0.063	0.563	0.125	0.031	0.625	0.125	0.063
Avg.	0.688	0.141	0.094	0.563	0.148	0.070	0.656	0.125	0.117
Max.	0.875	0.250	0.125	0.625	0.188	0.125	0.688	0.188	0.250

The length, height, and width of the stiffener undercuts listed in Table 2-4 were consistent among specimens 7C, 8C, and 9C. The average length, height, and depth of the stiffener undercuts were 0.04 in. (1 mm), 0.03 in. (0.8 mm), and 0.04 in. (1 mm). Similarly, the length, depth, and width of the flange undercuts listed in Table 2-5 were consistent among all three specimens. The average length, depth, and width of the flange undercuts were 0.64 in. (16 mm), 0.14 in. (3.6 mm), and 0.094 in. (2.4 mm).

Table 2-6: Specimen C Flange Grinding Surface Measurements (inches)

Undercut	7C		8C		9C	
I.D.	L	w	L	w	L	w
1E	3.00	0.075	4.00	0.070	5.00	0.055
2E	2.50	0.060	4.00	0.082	5.00	0.090

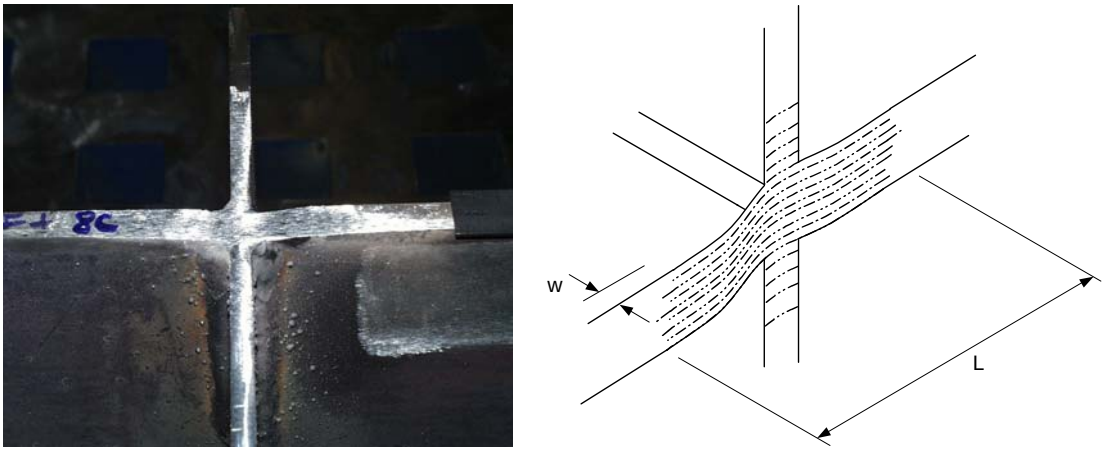

Figure 2-34: Specimen C Flange Grinding Surface Dimensions

After the undercuts were documented, a disk grinder was used to remove the flange undercuts. The repair was done on both sides of the flange. Prior to grinding, the flange undercuts were referred to as 1E, 2E, 3E, and 4E. Two surfaces are left after grinding. These surfaces correspond with locations 1E and 2E in Figure 2-33. Table 2-6 lists the post-grinding dimensions of the flange undercut locations. Figure 2-34 illustrates the flange grinding surface dimensions. The width, w, in Figure 2-34 was taken as the deepest point of grinding on the flange edge. The final slope of the grinding surface complies with specifications and is less than one in ten.

2.5.4 Type D Specimen Undercuts

Undercuts occurred exclusively at the exterior edge of the stiffener because the interior clip was fully welded as illustrated in Figure 2-35. The clip was minimized and then stiffener, flange, and web welds were overlapped to close the clip gap. Figure 2-36 shows the location and numbering of type D specimen undercuts.

Figure 2-35: Full Welding of Interior Clip

Table 2-7 lists the stiffener undercut dimensions corresponding to the locations in Figure 2-36. The average length, height, and depth of the stiffener undercuts were 0.05 in. (1.3 mm), 0.044 in. (1.11 mm), and 0.05 in. (1.3 mm) for specimens 10D, 11D, and 12D.

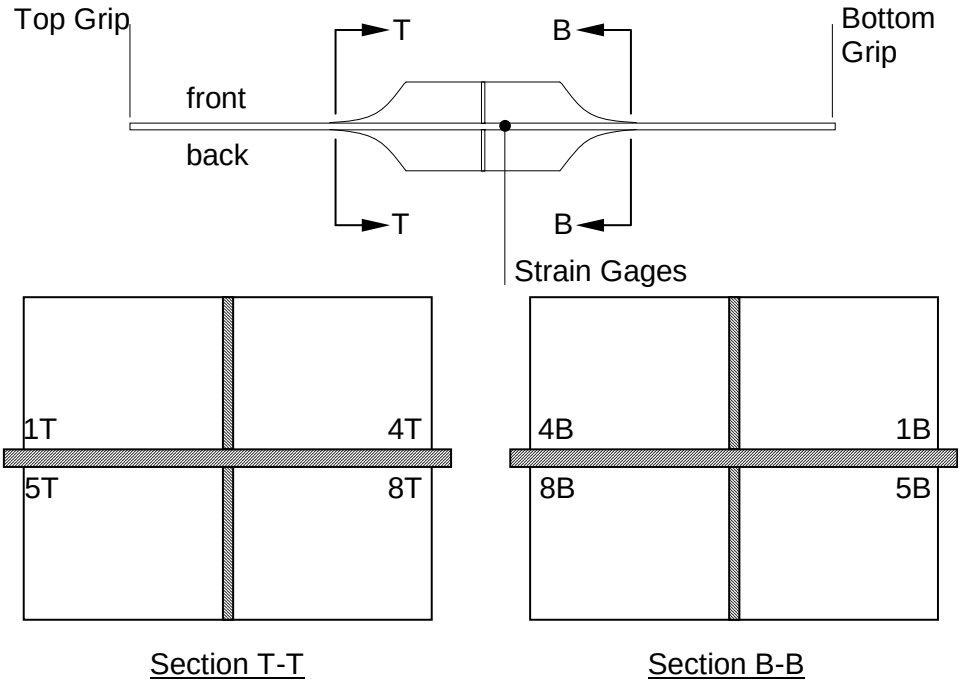

Figure 2-36: Specimen D Undercut Identification

Table 2-7: Specimen D Stiffener Undercut Measurements (inches)

Undercut	10D			11D			12D		
I.D.	L	h	d	L	h	d	L	h	d
1T	0.050	0.060	0.080	0	0	0	0.085	0.065	0.100
1B	0	0	0	0.075	0.075	0.075	0.050	0.050	0.050
4T	0.118	0.090	0.085	0.075	0.080	0.085	0.060	0.060	0.085
4B	0.050	0.050	0.050	0	0	0	0.080	0.090	0.090
5T	0	0	0	0.050	0.050	0.050	0	0	0
5B	0.110	0.100	0.125	0.060	0.075	0.050	0.050	0.050	0.065
8T	0	0	0	0	0	0	0.050	0.065	0.080
8B	0.180	0.100	0.125	0	0	0	0	0	0
Avg.	0.064	0.050	0.058	0.033	0.035	0.033	0.047	0.048	0.059
Max.	0.180	0.100	0.125	0.075	0.080	0.085	0.085	0.090	0.100

In summary, the interior and exterior stiffener undercuts were smaller than the flange undercuts. The average stiffener undercut dimensions for all specimens is listed in Table 2-8. The average length, height, and depth of the stiffener undercuts were approximately 0.05 in. (1.3 mm). However, there were several larger stiffener undercuts as was the case with specimen 2A and 7C. The average flange undercut dimensions for specimens B and C are also listed in Table 2-8. Depth of undercutting into the flange thickness was more severe than undercutting into the thickness of the stiffener.

Table 2-8: Average Undercut Dimensions

Undercut	L	h	d	w
Stiffener	0.058 (1.5 mm)	0.052 (1.3 mm)	0.047 (1.2 mm)	n/a
Flange	0.57 (14.5 mm)	n/a	0.13 (3.3 mm)	0.08 (2.0 mm)

The results of the fatigue tests are presented in the following chapter. The results showed that, despite the size of the stiffener and flange undercuts, no cracks initiated from an undercut location. This was the case for both large and small undercuts.

CHAPTER 3
Test Setup

3.1 INTRODUCTION

This chapter describes the test apparatus used for all research conducted during the project. The testing method and testing procedure are discussed in detail.

The specific welding detail in question is located on the tension flange of steel bridge girders. Vehicular traffic places the stiffener-to-flange connection in cyclic or pulsating loading, which may cause fatigue cracking.

Several test setups were considered in order to simulate these conditions. One option would be to create full-scale specimens and test them in four-point bending under repeated loading. The stiffener-to-flange connection would be located in the constant moment region and would be monitored for fatigue failures. Figure 3-1 illustrates the four-point test setup.

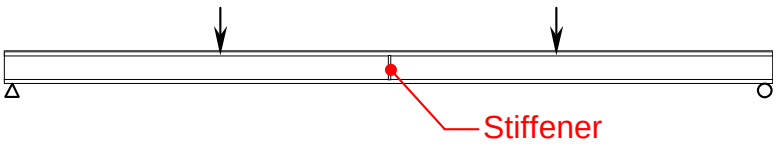

Figure 3-1: Four-point Bending

A second option would be to reproduce only the tension flange of the girder and the stiffener weldement. This assembly could then be tested under cyclic axial loading. The latter method was selected based on the availability of a uniaxial test frame located at the Ferguson Structural Engineering Laboratory. In addition, fabrication of smaller specimens is quicker and more economical in comparison to full-scale specimens.

3.2 TEST APPARATUS

An MTS uniaxial hydraulic testing machine was employed to test the specimens under cyclic loading. Pictured in Figure 3-2, the testing machine consists of a load frame, actuator, and upper and lower grips. The hydraulic ram is located below the lower grip and is out of view in Figure 3-2. A constant pressure hydraulic pump provides the power for the system.

Figure 3-2: MTS Uniaxial Testing Machine with Specimen

3.2.1 Test Frame Components

Pictured in Figure 3-3, an MTS hydraulic actuator with a 220 kips (979 kN) capacity was used to apply the test load. The actuator has a total stroke of 6 in. (152 mm), which was controlled by either a remote POD or the computer via the Testar II software. The actuator can be operated in either force or displacement control. Force control was used for all the tests.

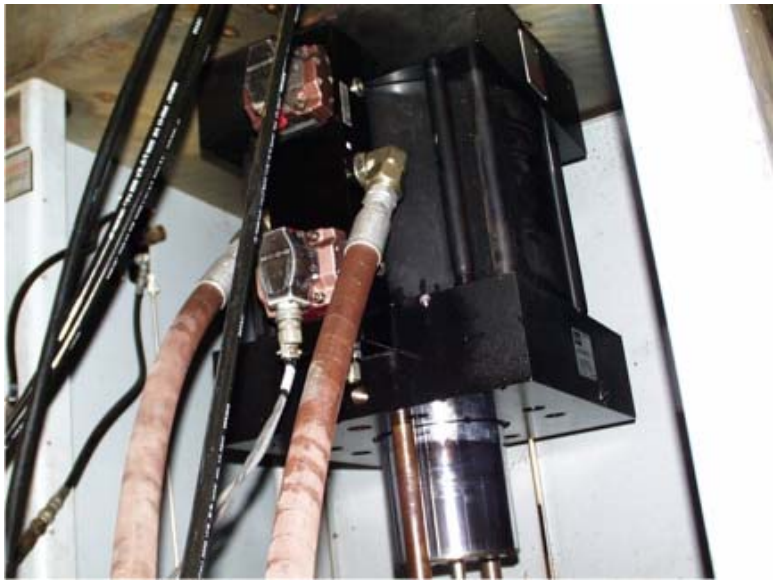

Figure 3-3: MTS Hydraulic Actuator

The test frame is equipped with custom upper and lower hydraulic grips (model 641.385) that have a load rating of 220 kips (979 kN). The grips are controlled using a hydraulic control module that regulates the gripping pressure. The specimens were gripped using a pressure of approximately 2500 psi. (17.2 MPa). Figure 3-4 displays photographs of both the hydraulic grip and the pressure control module.

Figure 3-4: Hydraulic Grip and Pressure Control Module

The MTS load frame (model 311.31) has a load rating of 220 kips (979 kN). The top crosshead can be raised and lowered as needed to accommodate a variety of specimen lengths. Once the proper length is determined, hydraulic rams on the top crosshead can be locked to fix the load frame in position.

3.2.2 Hydraulic Supply

An MTS hydraulic supply unit (model 506.20) was used to maintain pressure to the system throughout testing. The pump, pictured in Figure 3-5, supplies 20 gallons per minute (76 L/min.) at a constant pressure of 3000 psi (20.7 MPa). The pump was water cooled.

Figure 3-5: MTS Hydraulic Supply Unit

The pump is connected to a line conditioner that is controlled by the Teststar II system. The computer controlled Teststar system controls the hydraulic flow through the servo valve, making the appropriate corrections to maintain the desired test load. A schematic of the system is shown in Figure 3-6.

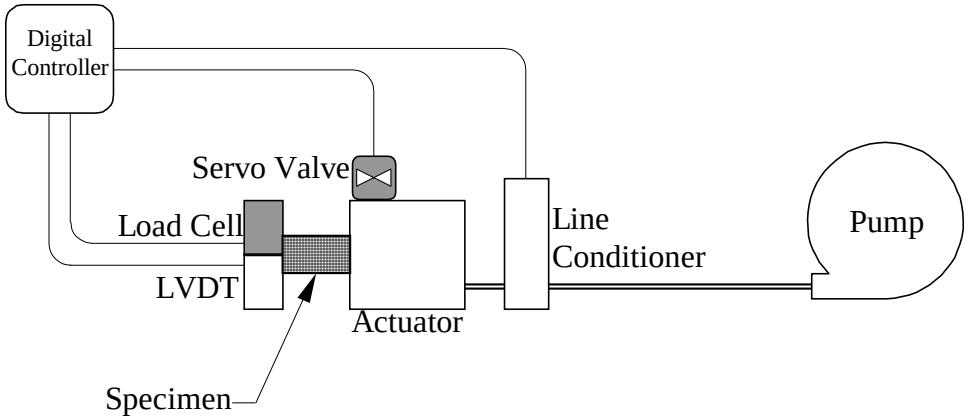

Figure 3-6: Hydraulic Schematic of Test System

3.3 TEST METHOD

All specimens were tested under cyclic axial tension with a minimum stress greater than zero. Test parameters and the step-by-step test procedure are discussed in this section.

3.3.1 Parameters

As previously discussed in Chapter 2.2, all specimens were tested under cyclic loading at a nominal stress range, S_R, of 20 ksi (138 MPa) and a stress ratio, R, of 0.2. The stress ratio is defined as the minimum nominal stress divided by the maximum nominal stress at the stiffener-to-flange connection. The minimum and maximum nominal stresses across the connection detail were 5 ksi (34.5 MPa) and 25 ksi (172 MPa), respectively.

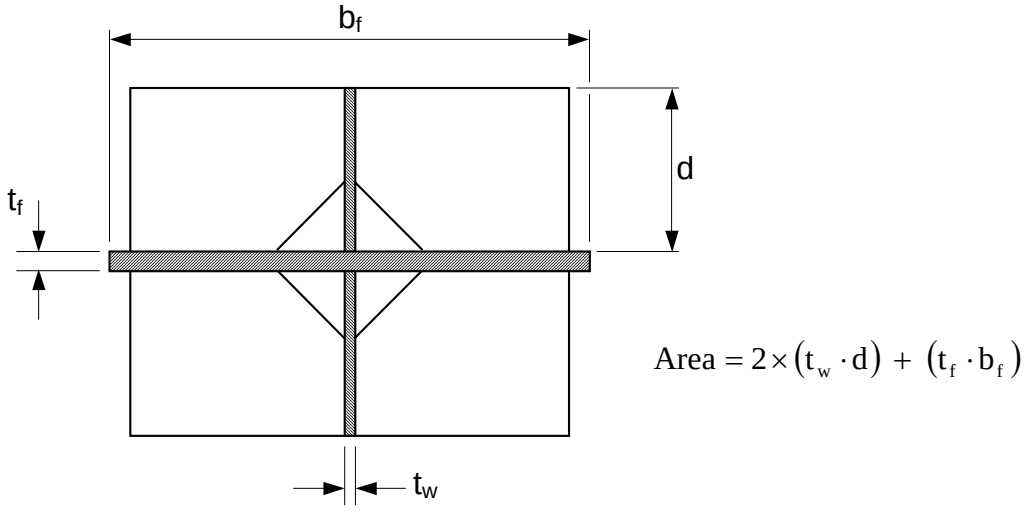

Figure 3-7: Area Used For Calculating Nominal Stress

The nominal stresses were calculated based on the area of the web plates and the flange plate as shown in Figure 3-7. The area is located adjacent to the

stiffener detail. The lower stress limit corresponded to an axial load of 35 kips (156 kN), whereas the upper stress limit was produced by an axial load of 175 kips (778 kN). Specimens were tested at either 1.50 Hz or 1.75 Hz. These frequencies were used to avoid a rocking instability of the test frame. Tests conducted at the reduced frequency of 1.50 Hz were done to limit the axial error feedback to approximately 5 kips (22 kN). This axial error limit was considered acceptable for all tests. The axial error occurred during transition from upper to lower limits and did not affect the maximum and minimum loads. The maximum and minimum loads were monitored and maintained throughout all testing. The error at the 175 kip maximum loading was less than 0.3 kips, a difference of less than 0.2% in applied load. The error at the 35 kip minimum loading was less than 0.2 kips, a difference of less than 0.6% in applied load. Figure 3-8 shows a graph of the applied load versus time.

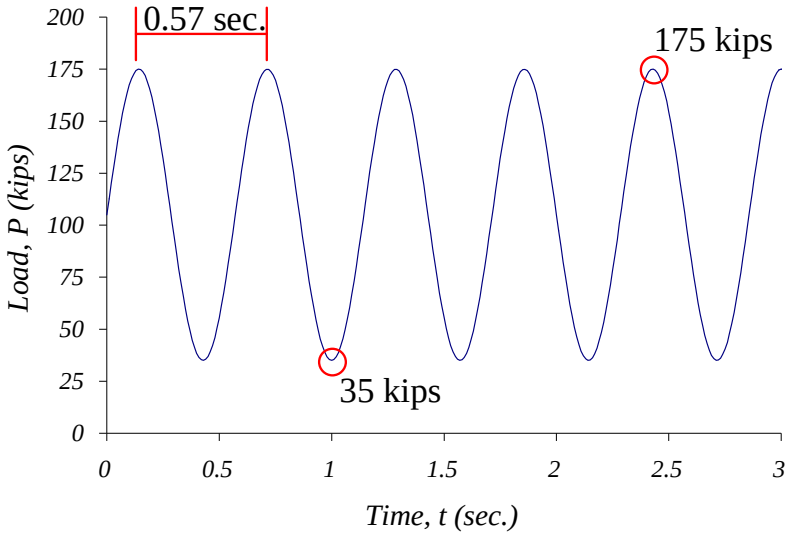

Figure 3-8: Experimental Applied Load versus Time

3.3.2 Test Procedure

Several steps were taken during the testing of each specimen in order to achieve accurate and consistent data. Each test consisted of preparation, specimen installation, testing and data monitoring, and specimen removal. Figure 3-9 shows a specimen installed in the test frame prior to loading.

Figure 3-9: Specimen Installed in Test Frame

3.3.2.1 Preparation and Precautions

In order to maintain safety and ensure proper testing, all parts of the test apparatus were thoroughly inspected prior to each test. All hydraulic lines were first inspected for leaks and then the cooling tower was turned on. The pump was then turned on and checked at both low and high operating pressures. The pump was next left on high pressure and the load frame was repeatedly raised and lowered along the column guides. This was done so that any residue and oils could be wiped from the columns using acetone to reduce the risk of load frame slippage during testing. Next, the actuator was jogged up and down using the POD control to ensure adequate oil flow during operation. The actuator was positioned to center stroke and both the displacement and force readings were

zeroed. As a final precaution, loose tools and lab equipment were cleared from the test frame.

3.3.2.2 Strain Gages

Prior to installation, several specimens were strain gauged and measured for plate thickness and width. Figure 3-10 shows the placement of the strain gages on the specimen. The gages were placed 2 in. (51 mm) from the centerline of the stiffener and 0.75 in (19 mm) on center from the edge of the specimen.

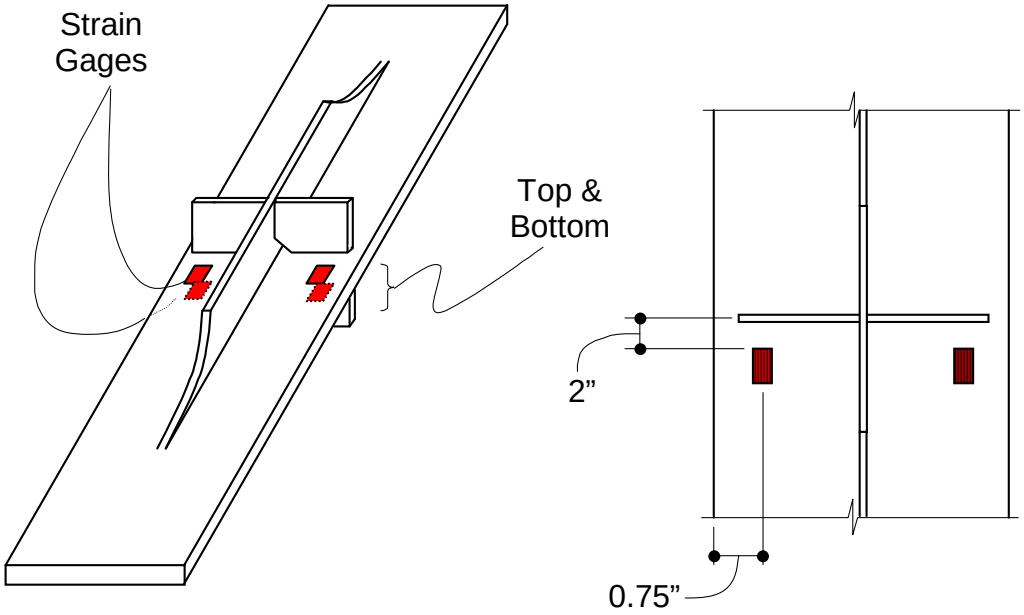

Figure 3-10: Arrangement of Strain Gages

3.3.2.3 Specimen Installation

Two people were employed to install the specimen into the lower grip of the machine. The top grip was next lowered onto the specimen. At this stage, neither grip was tightened or pressurized.

Next, the specimen was aligned in the grips. The top grip was then tightened and the specimen was raised so that the proper amount of plate was

gripped in the lower grip. Strain gage lead wires were then attached to the strain indicator. Once the strains were zeroed, the lower grip was tightened. A series of stepped static loads and corresponding strains were recorded on either side of the plate at the connection detail as shown in Figure 3-11.

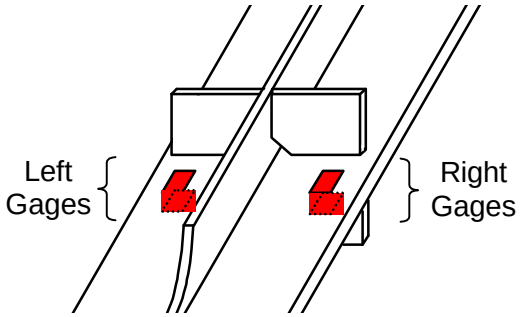

Figure 3-11: Strain Gage Pairings

Strain gage readings were taken to ensure proper alignment of the specimen to provide uniform stress distribution throughout the specimen. These tests were performed on eight of twelve total specimens. The resulting strain readings have been converted to stresses using a modulus of elasticity of 29000 ksi (200 MPa) and are summarized in Table 3-1 through Table 3-3. The upper and lower limit nominal stress readings are reported in Table 3-1 and Table 3-2, respectfully. The "left" tabulated values in Table 3-1 and Table 3-2 refer to the average of the top and bottom gage readings on the left side of the specimen. The "right" tabulated values in Table 3-1 and Table 3-2 refer to the average of the top and bottom gage readings on the right side of the specimen. It can be seen from Table 3-1 that the upper limit stress is approximately 25 ksi. Likewise, Table 3-2 shows that the lower limit stress is approximately 5 ksi. Table 3-3 lists the average of the four strain gage readings. It can be seen from Table 3-3 that the stress range is approximately 20 ksi. The strain gage readings were consistent with the nominal stress range of 20 ksi (138 MPa) across the stiffener-to-flange connection.

Table 3-1: 25 ksi Upper Stress Limit Readings

Specimen Number	Maximum Gage Stress (ksi)		
	Left	Right	Average
5B	26.46	26.30	26.38
6B	26.17	25.91	26.04
7C	26.01	26.07	26.04
8C	25.87	26.39	26.13
9C	26.22	25.40	25.81
10D	25.27	25.10	25.19
11D	23.53	25.32	24.43
12D	24.45	24.87	24.66

Table 3-2: 5 ksi Lower Stress Limit Readings

Specimen Number	Minimum Gage Stress (ksi)		
	Left	Right	Average
5B	5.38	5.24	5.31
6B	5.26	5.14	5.20
7C	5.22	5.16	5.19
8C	5.24	5.10	5.17
9C	5.20	5.12	5.16
10D	4.99	5.08	5.03
11D	4.69	4.85	4.77
12D	4.85	4.87	4.86

Table 3-3: Average Upper & Lower Limit Stress Readings

Specimen Number	Average Gage Stress (ksi)		
	Minimum	Maximum	S_r
5B	5.31	26.38	21.07
6B	5.20	26.04	20.85
7C	5.19	26.04	20.86
8C	5.17	26.13	20.96
9C	5.16	25.81	20.65
10D	5.03	25.19	20.15
11D	4.77	24.43	19.65
12D	4.86	24.66	19.80

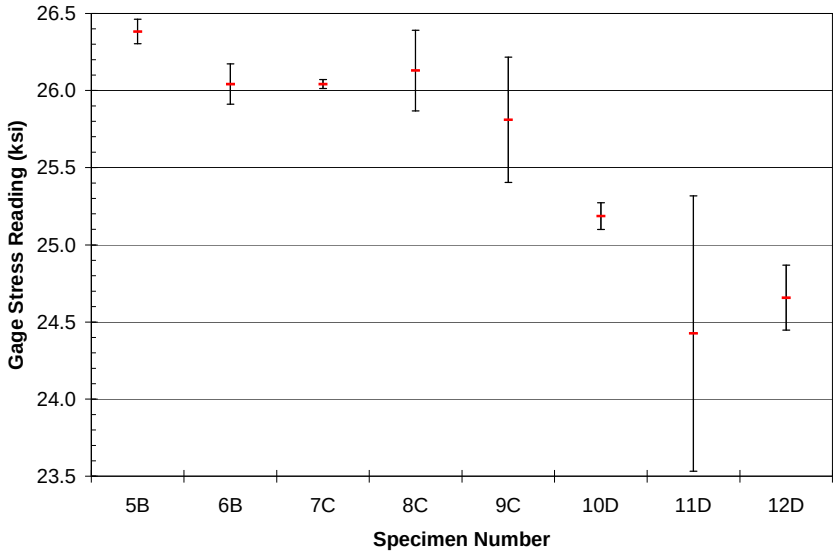

Figure 3-12: Left, Right, & Average Upper Stress Limit Readings

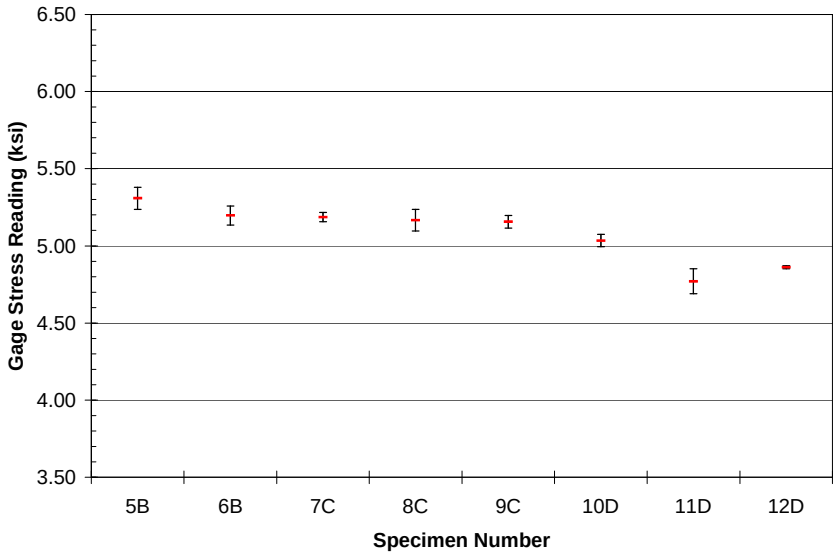

Figure 3-13: Left, Right, & Average Lower Stress Limit Readings

Figure 3-12 shows the difference between the left and right stress readings for the upper limit stress of 25 ksi. With the exception of specimen 11D, the difference between the left and right upper limit stress readings is less than 3.5% for all specimens. The difference between the left and right stress readings for specimen 11D is approximately 7%. Figure 3-13 shows the difference between the left and right stress readings for the lower limit stress of 5 ksi. The difference between the left and right upper limit stress readings is less than 3.5% for all eight specimens. All differences were considered acceptable.

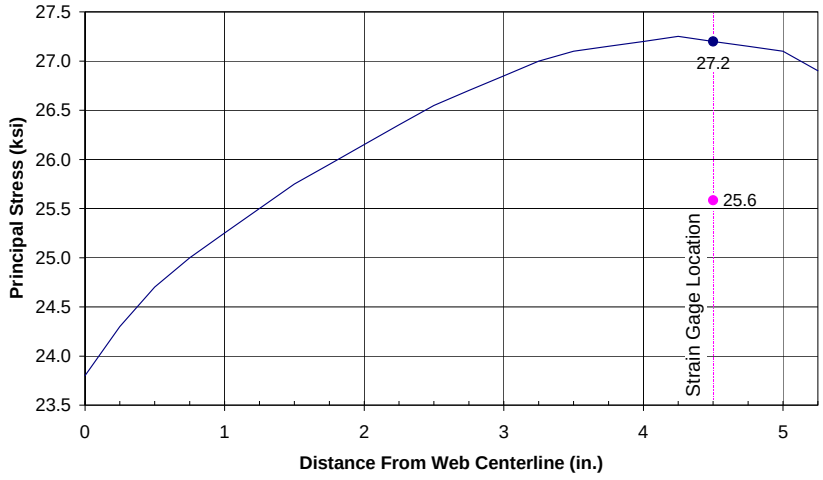

Figure 3-14: Gage Stress versus Finite Element Flange Stress

The readings in Table 3-1 through Table 3-3 confirm the stress results of the finite element model discussed in Chapter 2.2.1. The cumulative average of the maximum gage stress readings from Table 3.1 is 25.6 ksi (177 MPa). The finite element model results in Figure 3-14 show that the principal stress under maximum loading conditions is 27.2 ksi (188 MPa) at the same location as the strain gage readings. These values are highlighted in Figure 3-14. In addition, the cumulative average of the stress range values in Table 3.3 is 20.5 ksi (141 MPa). In comparison, the finite element model average stress range in the flange

was 21 ksi (145 MPa). Therefore, the gage readings and finite element model are in acceptable agreement with the nominal stresses.

3.3.2.4 Testing and Data Monitoring

The loads and operating frequency were next entered into the computer via the Testar II software. The loads and operating frequency were achieved through smaller increments, bringing the machine up to speed at a controlled rate. Once the test had reached the target loads and operating frequency, error detectors were set to prevent damage to either the machine or the specimen. The error detectors were used to monitor changes in force or displacement such as failure of the specimen. In addition, these error detectors were used to guard against unwanted events such as voltage spikes.

A log was also kept for each test. The number of cycles, maximum and minimum forces, maximum and minimum displacements, and axial error were all recorded on a daily basis. Additionally, the pump temperature was closely monitored to prevent overheating of the system. Furthermore, close inspection of the specimen itself was conducted daily to identify any visible signs of cracking.

3.3.2.5 Specimen Removal

Specimens were considered failed if either (1) an error detector was triggered by an increase in specimen displacement of 0.10 in. (2.54 mm) due to a crack opening or (2) rupture occurred due to rapid crack propagation. When triggered, the detectors were set to immediately stop all testing by turning off the hydraulics. The specimens were then carefully ungripped and removed from the machine. Exposed fracture surfaces were immediately sprayed with a protective clear acrylic to prevent subsequent corrosion. The fatigue life was then marked on each specimen and recorded in the log.

CHAPTER 4
Fatigue Test Results

4.1 INTRODUCTION

The results of the fatigue tests are discussed in this chapter. The fatigue life, or number of loading cycles to failure, was recorded and is presented for each specimen. All specimens were tested at a nominal stress range, S_R, of 20 ksi (138 MPa). A post mortem analysis of the specimens and photographs of the fracture surfaces are included. An analysis of variance was performed on the data to detect the differences, if any, among the fatigue performances of the specimen types.

The test results given in this chapter confirm that specimen failure was independent of undercutting at both the stiffener and flange. Failure of the specimens was found to occur along the stiffener-to-flange weld toe. The likely failure path of the specimens is shown in Figure 4-1. Figure 4-1 shows that the fatigue cracks initiated at the stiffener-to-flange weld toe and propagated into the thickness of the flange. Secondary cracks may begin to form at other weld toe locations, but failure ultimately occurs due to the reduction in area as the cracks continue to propagate into the flange.

Four stages of cracking are shown in Figure 4-1. A close-up of stage 1 crack section is shown in Figure 4-2. Smaller cracks form at the weld toe and eventually coalesce in stage 2 to form a larger, shallow fatigue crack as shown in Figure 4-3. In stage 3, the crack continues to grow through the flange as shown in Figure 4-4. The crack growth is quicker along the surface of the flange due to the large stress concentration at the weld toe.

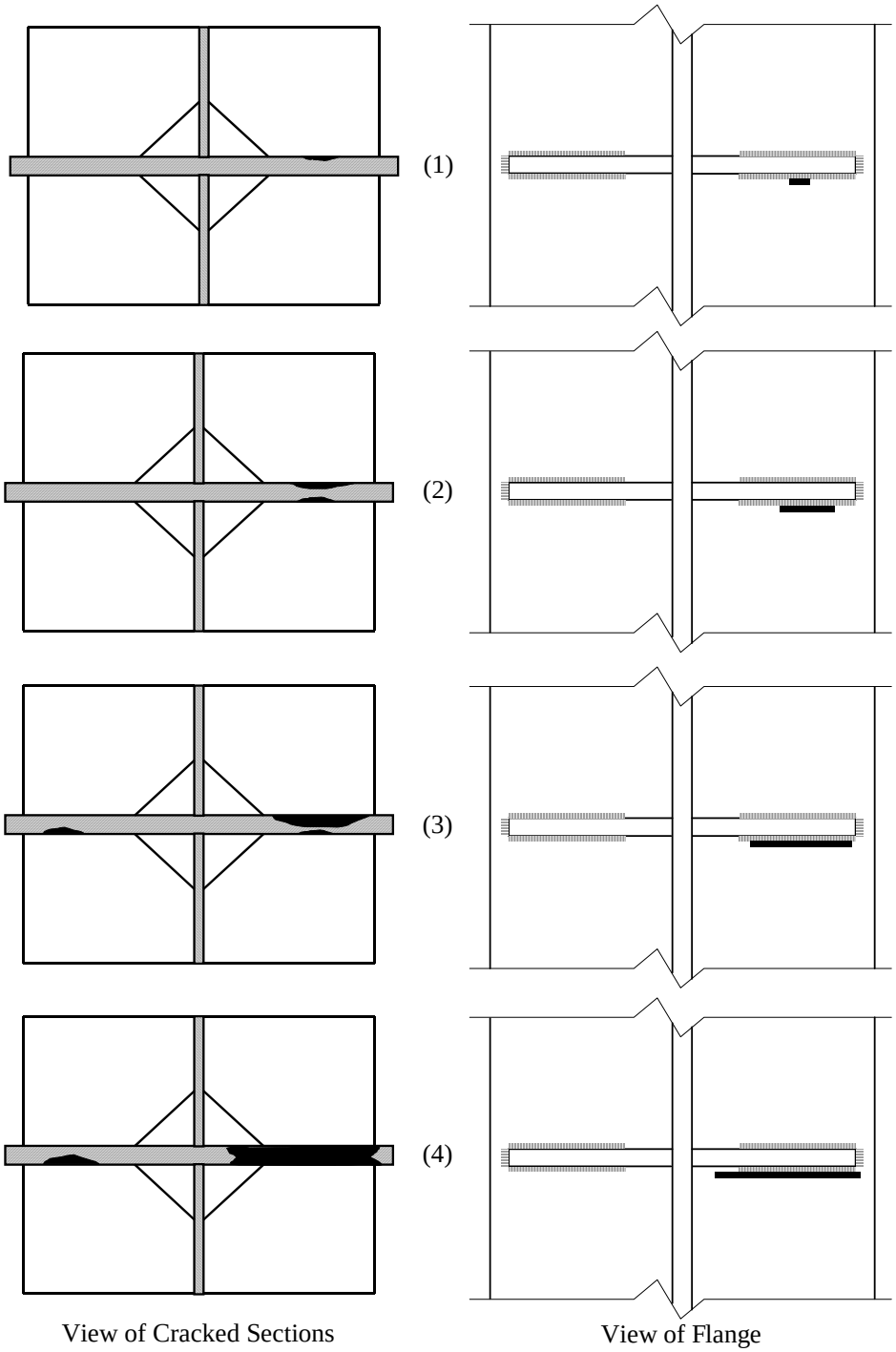

Figure 4-1: Failure Path by Stage Number

Crack growth becomes more rapid in Stage 4. Figure 4-5 shows the double-edged crack expanding along the length of the weld toe. Eventually, the remaining flange edge will tear and the fatigue crack will rapidly propagate across the rest of the flange. Figure 4-6 shows the resulting single-edged crack propagation leading to failure of the specimens.

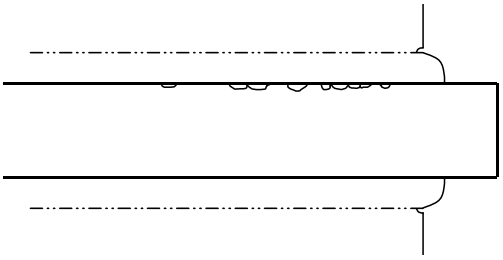

Figure 4-2: Stage 1

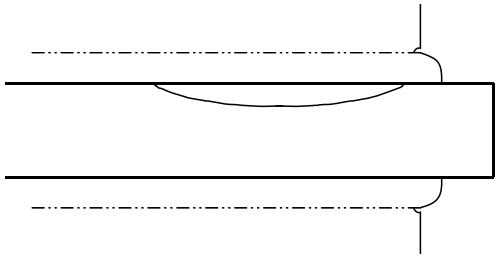

Figure 4-3: Stage 2

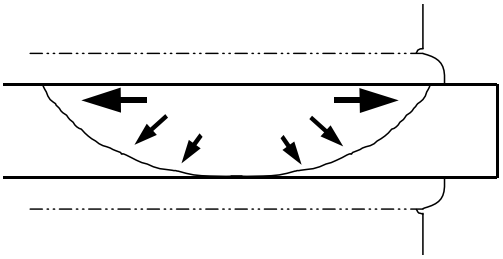

Figure 4-4: Stage 3

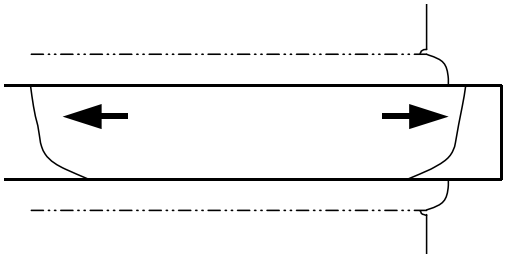

Figure 4-5: Stage 4

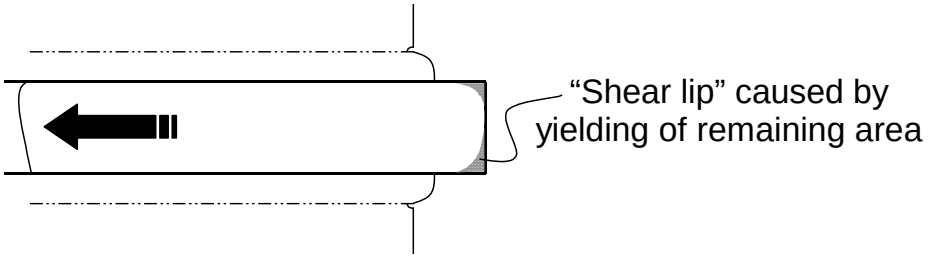

Figure 4-6: Failure

4.2 SPECIMEN RESULTS

Table 4-1 summarizes the fatigue test results of the specimens. The resulting fatigue life of the specimens and the corresponding average measured stress range values discussed in Chapter 3.3.2.3 are shown in Table 4-1. The average fatigue life of each specimen type is also listed in the table.

Table 4-1: Summary of Fatigue Testing Results

Specimen		Stress Range S_R (ksi)	Cycles to Failure N_f	Average Cycles to Failure
Clip Opening Short stiffener	1A	20*	508,199	459,271
	2A	20*	439,185	
	3A	20*	430,429	
Clip Opening Long stiffener	4B	20*	212,662	448,339
	5B	21.1	628,377	
	6B	20.8	503,978	
Clip Opening Long stiffener repaired	7C	20.9	574,097	479,544
	8C	21.0	435,863	
	9C	20.7	428,672	
No Clip Opening Short stiffener	10D	20.2	559,106	422,978
	11D	19.7	492,794	
	12D	19.8	217,035	
Average		20.5**		452,533

*not measured; nominal S_R=20 ksi

**does not include nominal values 1A through 4B

Specimen 5B had the longest fatigue life, failing at 628,377 cycles of loading at a measured stress range of 21.1 ksi (145 MPa). Specimen 4B had the shortest fatigue life, failing at 212,662 cycles. A nominal stress range of 20 ksi was assumed for specimen 4B since the first four specimens were not strain gauged. The average fatigue life of all specimens tested was 452,533 cycles. The

average measured stress range was 20.5 ksi (141 MPa), excluding specimens 1A, 2A, 3A, and 4B.

Fatigue cracks and fracture surfaces are discussed in the following sections.

4.2.1 Recording of Fatigue Cracks

The system used for recording the fracture locations is similar to the method implemented for recording undercut locations (refer to Chapter 2.5). Crack locations correspond to the numbering of stiffener-to-flange welds as illustrated in Figure 4-7. Therefore, fatigue cracks and initiation points were referenced to a particular weld number shown in Figure 4-7. All twelve specimens follow this scheme.

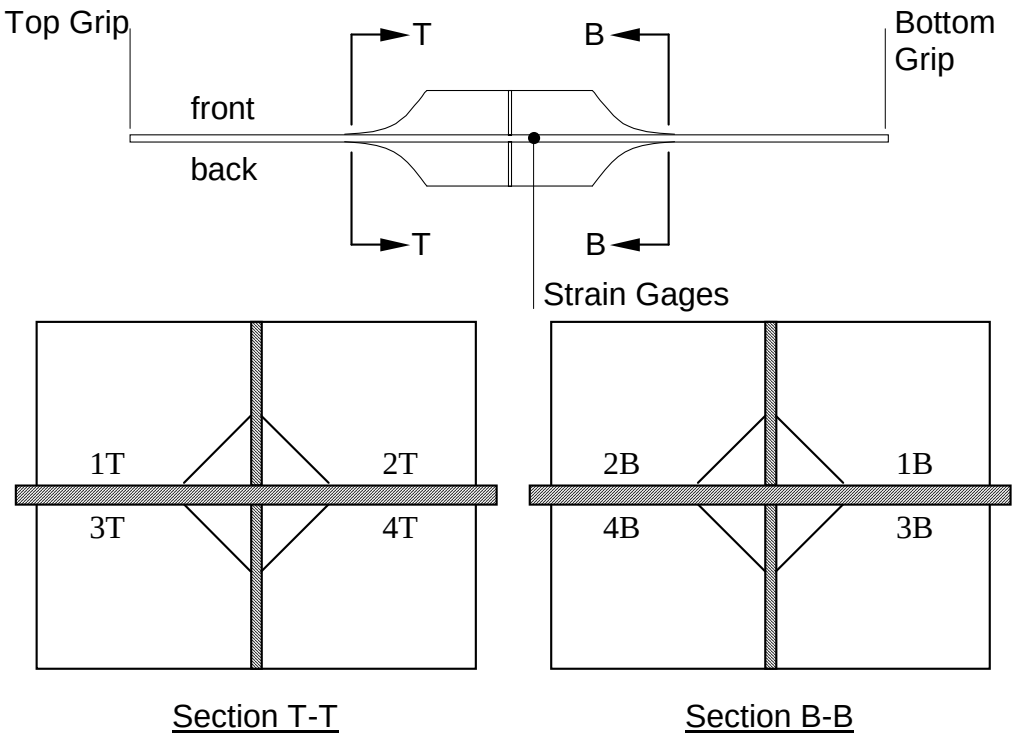

Figure 4-7: Stiffener-to-Flange Weld Numbering

Table 4-2 lists the weld locations where cracking occurred for specimens 1A through 12D. All failures occurred due to fatigue cracking along the weld toe. Seven specimens exhibited fatigue cracking at weld location 4T. It should be noted that specimens 2A and 3A had a fatigue crack form at a radial web taper. These cracks were caused by weld start-stops (refer to Chapter 2.3.2) along the web-to-flange welds.

Table 4-2: Specimen Failure Locations

Specimen Number	Weld Location							
	1T	2T	3T	4T	1B	2B	3B	4B
1A	●	●		●				
2A*								
3A**				●		●		
4B				●				
5B		●		●				
6B					●	●	●	●
7C		●		●	●		●	
8C		●		●				
9C					●		●	
10D						●		●
11D	●		●	●				
12D			●					

*crack at bottom web taper
**crack at top web taper

4.2.2 Fracture Surfaces

Figure 4-8 illustrates the fracture surface numbering scheme. A failed specimen is shown in Figure 4-8. Fracture surfaces are labeled according to either the top or bottom grip. Fracture surface 1 is always viewed looking toward the upper grip, and fracture surface 2 is viewed looking toward the bottom grip. All fracture surface photographs in the following sections were taken with the front flange surface (see Figure 4-7) of the specimen facing up.

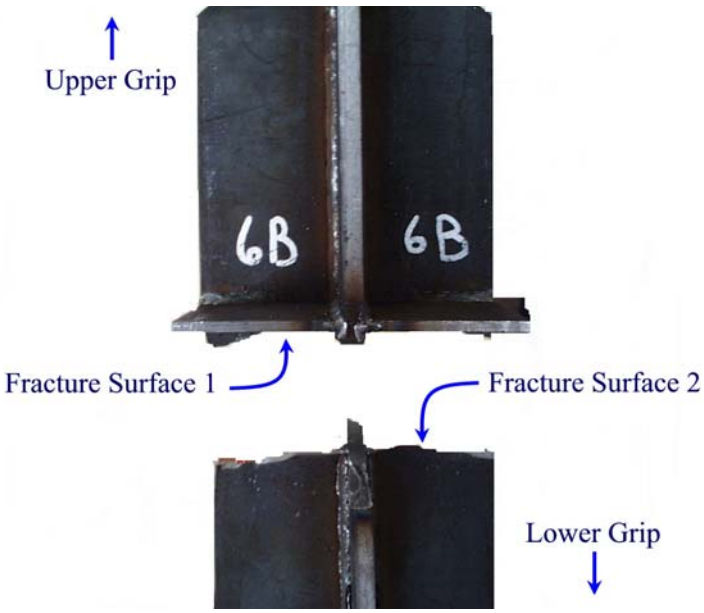

Figure 4-8: Fracture Surface Numbering

Stage 2 and 3 fatigue cracks (refer to Figures 4-3 and 4-4) are identified by their smooth elliptical shapes. Remaining areas are coarse in appearance, indicating the more rapid crack extension of Stage 4 (refer to Figure 4-5). The extent of fatigue cracking was highlighted in some of the figures using dashed lines. Stars are used indicate the crack initiation points along the weld toe. Select specimens are discussed in the following paragraphs.

Specimen 1A was tested at a nominal stress range of 20 ksi (138 MPa). The actual stress range for specimen 1A was not measured. Specimen 1A failed at 508,199 cycles due to fatigue cracks at the toe of the stiffener-to-flange weld locations 1T, 2T, and 4T. Failure occurred as these cracks propagated into the flange causing total rupture of the cross-section by yielding. No cracks were found to have initiated at an undercut location.

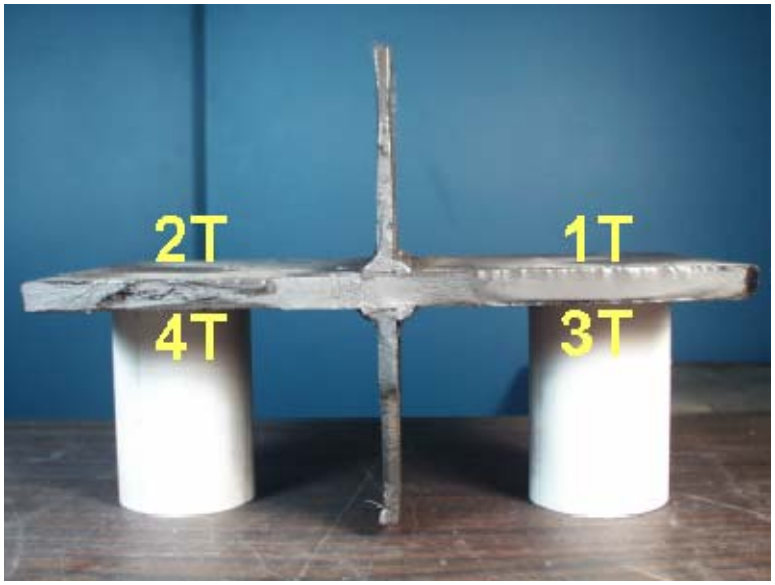

Figure 4-9: Fracture Surface 1A-1

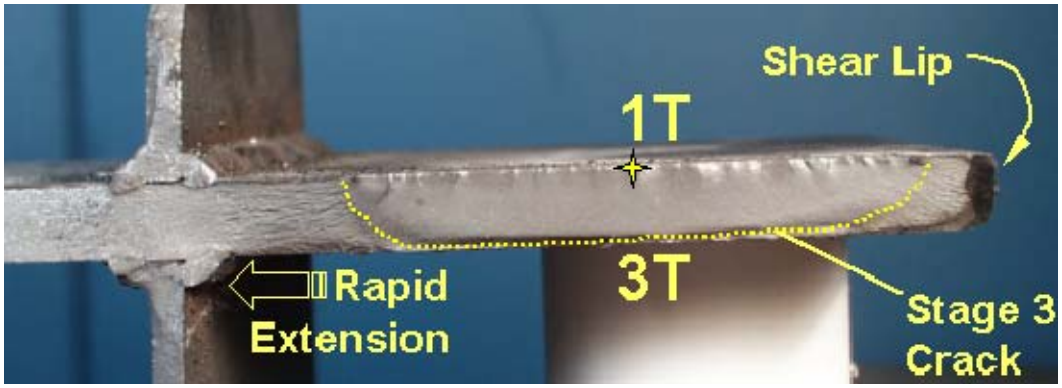

Figure 4-10: 1A-1 Cracks at Toe of Welds 1T and 3T

Fracture surface 1 is shown in Figure 4-9. Weld locations are numbered in the figure. The large elliptical crack on the right half of the photograph in Figure 4-9 occurs at the toe of weld 1T. A close-up of this crack is shown in Figure 4-10. Stage 3 of the crack (refer to Figure 4-4) is highlighted in the figure. Following this stage, yielding of the edge of the flange occurred as evidenced by the shear lips in Figure 4-10. Rapid crack propagation took place in stage 4 and failure occurred. Note the change in texture from a smooth surface in Stage 3 to a more roughened surface in Stage 4.

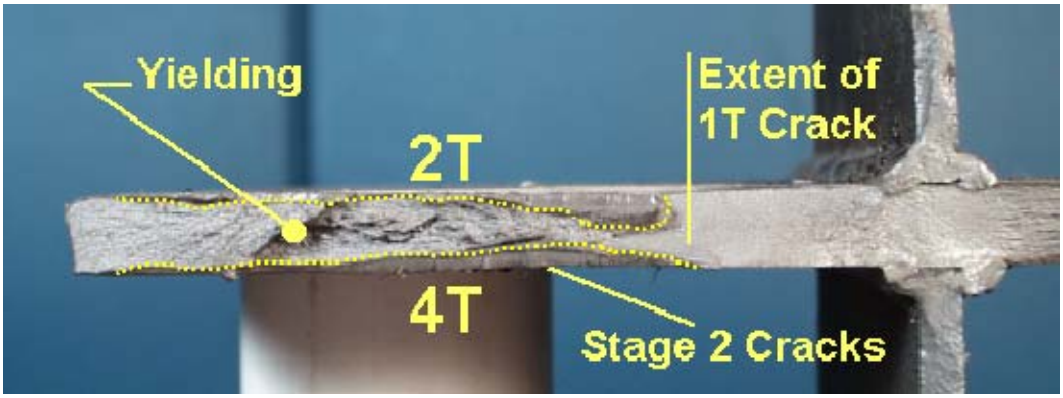

Figure 4-11: 1A-1 Cracks at Toe of Weld 1T

The smaller cracks on the left side of Figure 4-9 occur at the toe of welds 2T and 4T. A close-up of these cracks is shown in Figure 4-11. These cracks were in stage 2 of their development when rupture of the specimen occurred due to the rapid crack extension of the crack at weld toe 1T.

Specimen 2A was tested at a nominal stress range of 20 ksi (138 MPa). The actual stress range for specimen 2A was not measured. Specimen 2A failed at 439,185 cycles due to a fatigue crack at the bottom radial web taper as Shown in Figure 4-12. No visible cracks were found at an undercut location.

Figure 4-12: Fracture Surface 2A-1

The crack propagated into the flange from a weld start-stop. The start-stop acted as an initial flaw in the web-to-flange weld and continued to grow during testing. Figure 4-13 shows the initiation points at the weld start-stop. The crack was believed to grow downward into the flange from these initiation points causing a severe decrease in area resulting in rupture of the specimen.

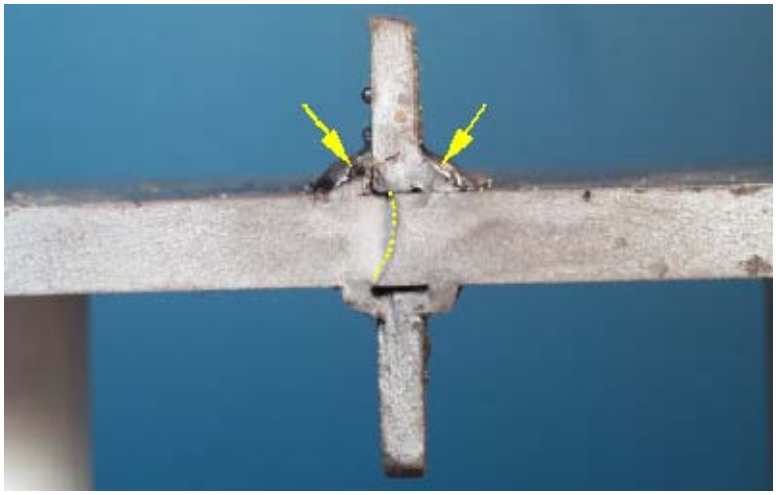

Figure 4-13: 2A-2 Showing Flaws at Start-Stop

Specimen 3A was tested at a nominal stress range of 20 ksi (138 MPa). The actual stress range for specimen 3A was not measured. Specimen 3A failed at 430,429 cycles due to fatigue cracks at the toe of the stiffener-to-flange weld locations 4T and 4B as shown in Figure 4-14. In addition, a third crack formed at the upper radial web taper as shown in Figure 4-15. This crack formed due to a weld stop-start in the web-to-flange weld (similar to specimen 2A). A specimen displacement over the 0.10 in. limit halted the actuator prior to total rupture of the specimen. No cracks were found to have initiated at an undercut location.

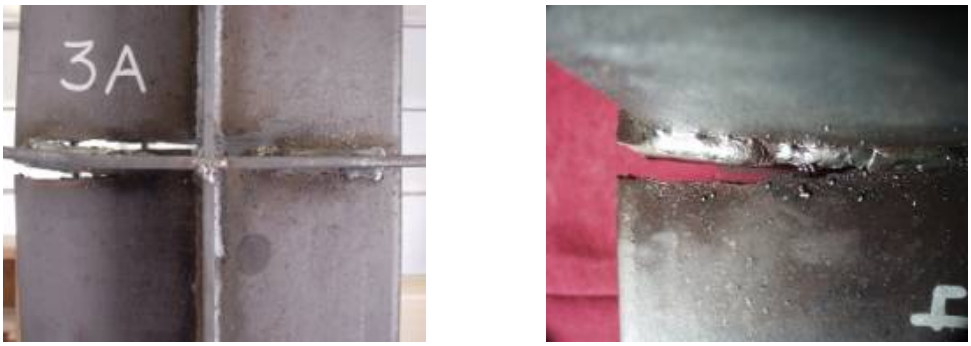

Figure 4-14: Multiple Cracks at Toe of Welds 4T and 4B

Figure 4-15: Crack at Upper Radial Web Taper

Failure at the radial tapers in specimens 2A and 3A led to revisions in the welding sequence. A new welding sequence and repairs were employed to eliminate failures at weld start-stop locations. Refer to Chapter 2.3.2 for details.

Specimen 5B was tested at a measured stress range of 21.1 ksi (145 MPa). Specimen 5B failed at 628,377 cycles due to fatigue cracks at the toe of the stiffener-to-flange weld locations 2 and 4. Figure 4-16 shows the toe crack along weld location 2T. A displacement over the 0.10 in. limit halted the actuator prior to total rupture of the specimen.

Figure 4-16: Crack at Toe of Weld 2T

Figure 4-17 shows the fracture surface near the edge flange undercuts. It can be seen that the crack does not start at the undercut. Figure 4-17 shows that ductile tearing of the flange edge occurred due to crack growth from weld toe 2T. In addition, the fracture surface conforms to the shape of the undercut because the weld metal is harder than the base metal.

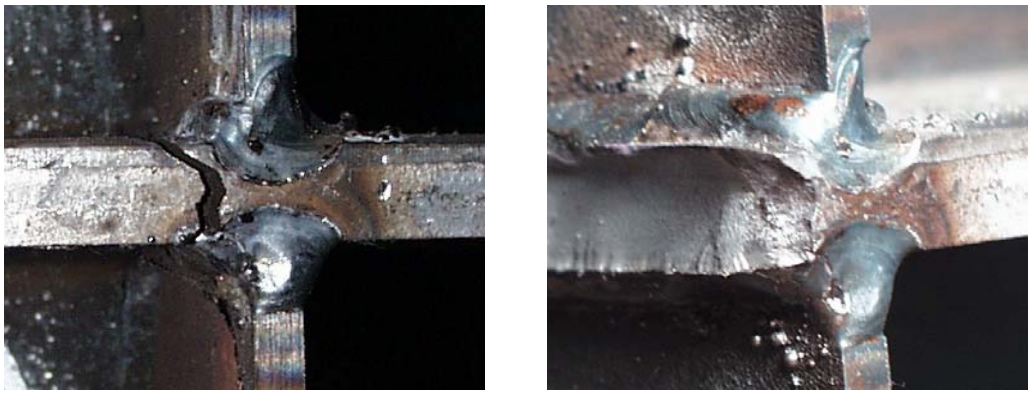

Figure 4-17: Ductile Tear of Flange Edge

Specimen 6B was tested at a measured stress range of 20.8 ksi (143 MPa). Specimen 6B failed at 503,978 cycles due to fatigue cracks at the toe of the stiffener-to-flange weld locations 1B, 2B, 3B, and 4B. Failure occurred as these cracks propagated into the flange causing total rupture of the cross-section by yielding. No cracks were found to have initiated at an undercut location.

Figure 4-18 shows fracture surface 1. Fatigue cracks are shown growing from the toe of the stiffener-to-flange welds. Figure 4-19 and Figure 4-20 show close-up views of these fatigue cracks.

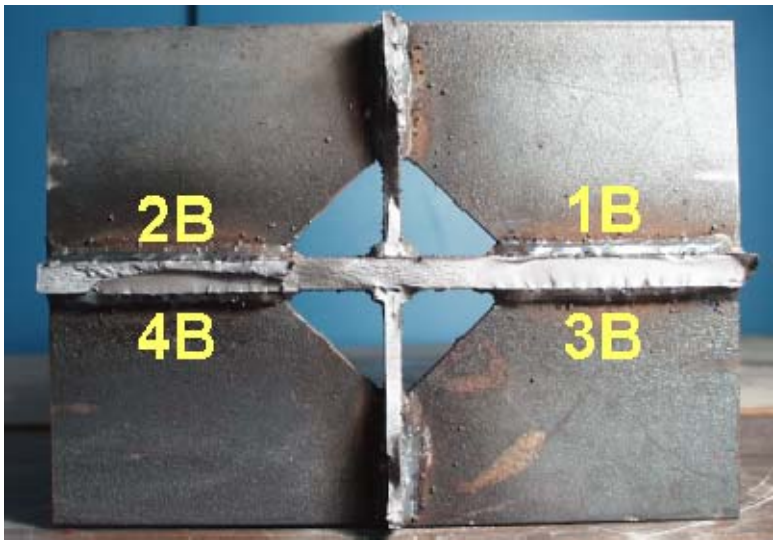

Figure 4-18: Fracture Surface 6B-1

Figure 4-19 shows both a large crack at weld toe 3T and smaller cracks at weld toe 1T. The larger crack ultimately caused failure of the specimen as is propagated across the flange. Again, notice the change in texture as the crack extends over to weld locations 2B and 4B. Figure 4-20 shows a series of smaller cracks coalescing at the toe of weld 2B. In addition, a larger crack propagated upward from weld toe 4B. Yielding occurred between cracks 2B and 4B during specimen failure. Note the crack growth from weld toe 3B on the right in Figure 4-20.

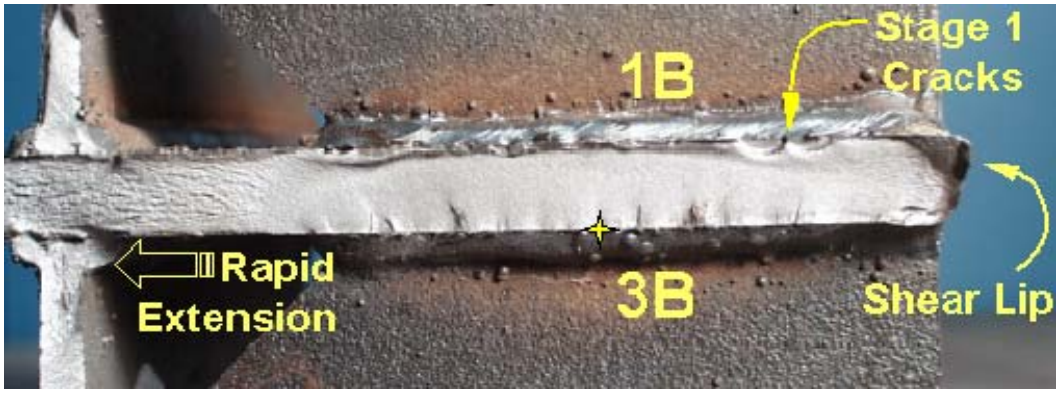

Figure 4-19: 6B-1 Crack at Toe of Welds 1B and 3B

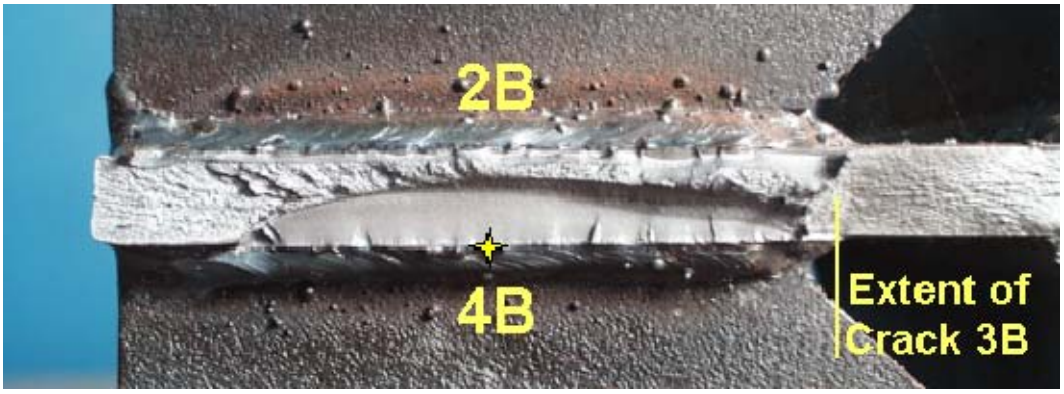

Figure 4-20: 6B-1 Crack at Toe of Welds 2B and 4B

Specimen 7C was tested at a measured stress range of 20.9 ksi (144 MPa). Specimen 7C failed at 574,097 cycles due to fatigue cracks at the toe of the stiffener-to-flange weld locations 2T, 4T, 1B, and 3B. Failure occurred as these cracks propagated into the flange causing total rupture of the cross-section by yielding. Some stiffener welds were also ruptured during failure as shown in Figure 4-21. No cracks were found to have initiated at an undercut location.

Figure 4-21: Failure of Specimen 7C

Figure 4-22 shows fracture surface 1. Note that welds 2T and 4T do not share the same plane as welds 1B and 3B. Fatigue cracks in Figure 4-23 originated from the toe of the stiffener-to-flange weld toe at weld locations 2T and 4T. Fatigue cracks in Figure 4-24 originated from the toe of the stiffener-to-flange weld toe at weld locations 1B and 3B.

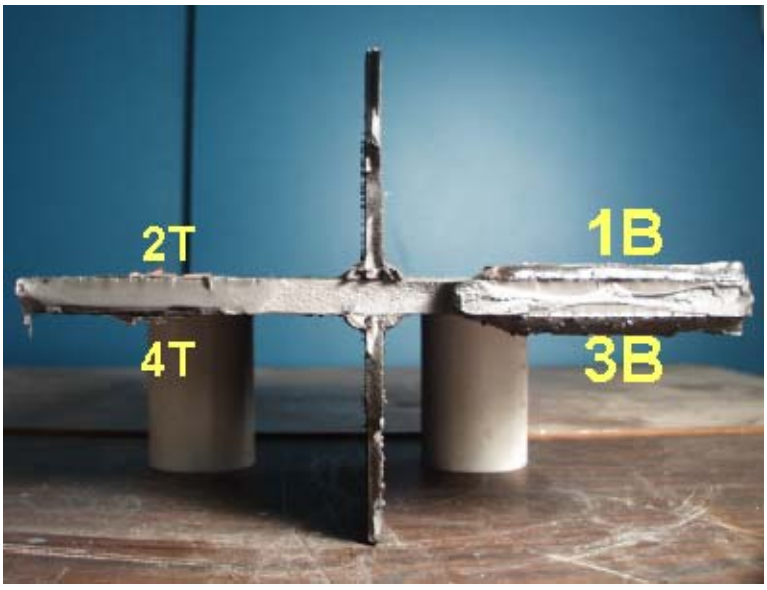

Figure 4-22: Fracture surface 7C-1

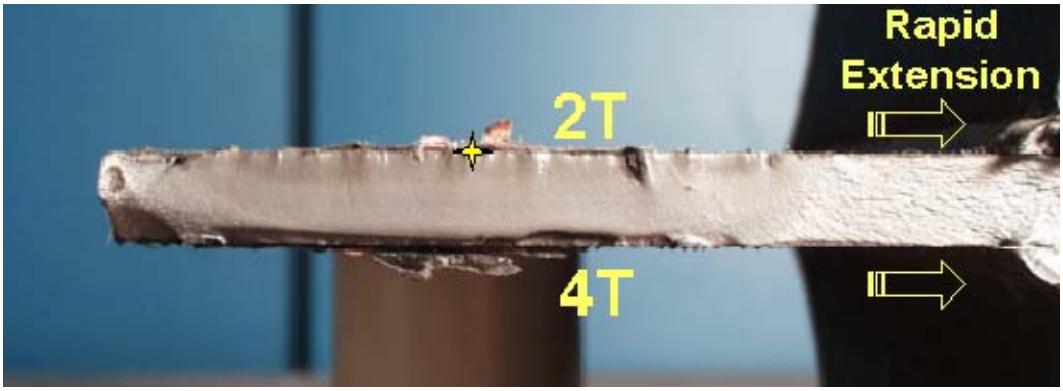

Figure 4-23: 7C-1 Crack at Toe of Welds 2T and 4T

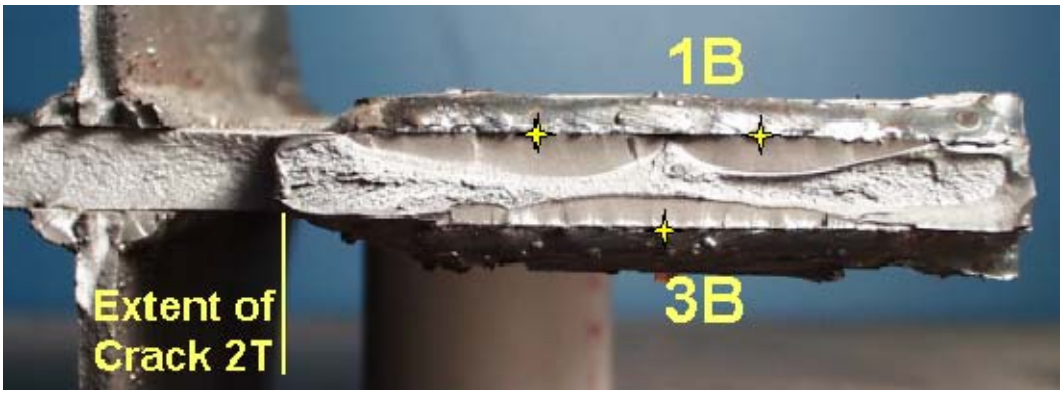

Figure 4-24: 7C-1 Crack at Toe of Welds 1B and 3B

Specimen 8C was tested at a measured stress range of 21 ksi (145 MPa). Specimen 8C failed at 435,863 cycles due to fatigue cracks at the toe of the stiffener-to-flange weld locations 2T and 4T. Figure 4-25 shows the toe crack along weld location 2T. A displacement over the 0.10 in. limit halted the actuator prior to total rupture of the specimen. No cracks were found to have initiated at an undercut location.

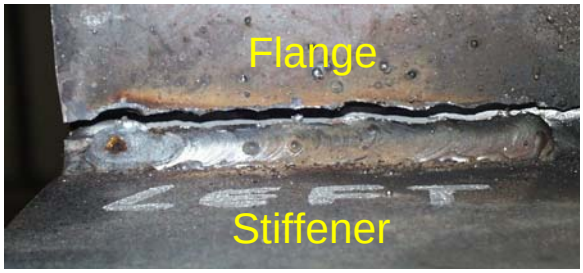

Figure 4-25: Specimen 8C Weld 2T Toe Crack

Specimen 11D was tested at a measured stress range of 19.7 ksi (136 MPa). Specimen 11D failed at 492,794 cycles due to fatigue cracks at the toe of the stiffener-to-flange weld locations 1T, 3T, and 4T. A displacement over the 0.10 in. limit halted the actuator prior to total rupture of the specimen. No cracks were found to have initiated at a stiffener undercut location.

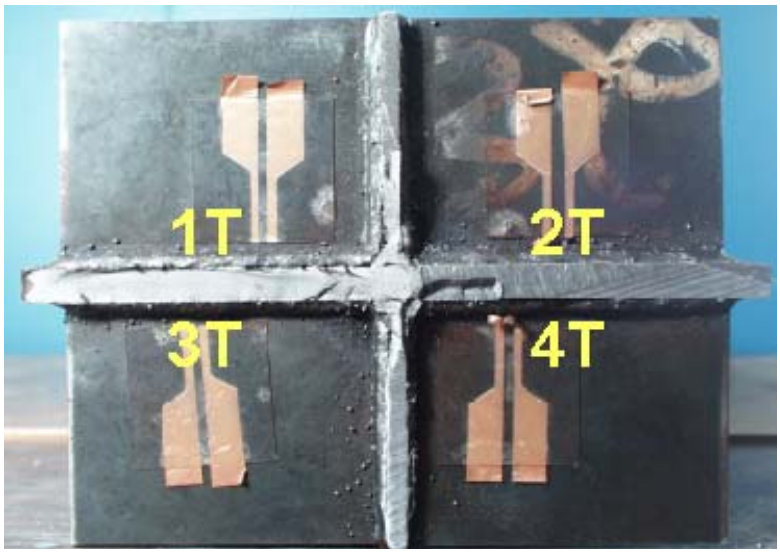

Figure 4-26: Fracture Surface 11D-2

Figure 4-26 shows fracture surface 2. A close-up of the fatigue cracks at the toe of welds 1T and 3T is shown in Figure 4-27. A shear lip is also indicated in the figure. Again, this specimen follows the same failure sequence as discussed in section 4.1.

Figure 4-28 shows the center of the fracture surface including the cracks at the toe of weld 4T. Recall that the stiffener clip was eliminated for type D specimens. As a result, cracks grew further along the toe of the stiffener-to-flange weld closer to the centerline of the specimen as shown in Figure 4-28. It should be noted that the fracture surfaces of specimens 10D and 12D were similar to the fracture surface of 11D.

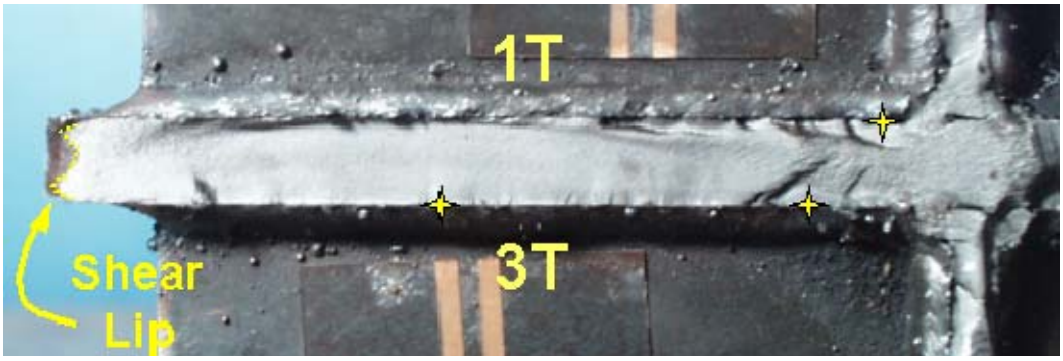

Figure 4-27: 11D-2 Crack at Toe of Welds 1T and 3T

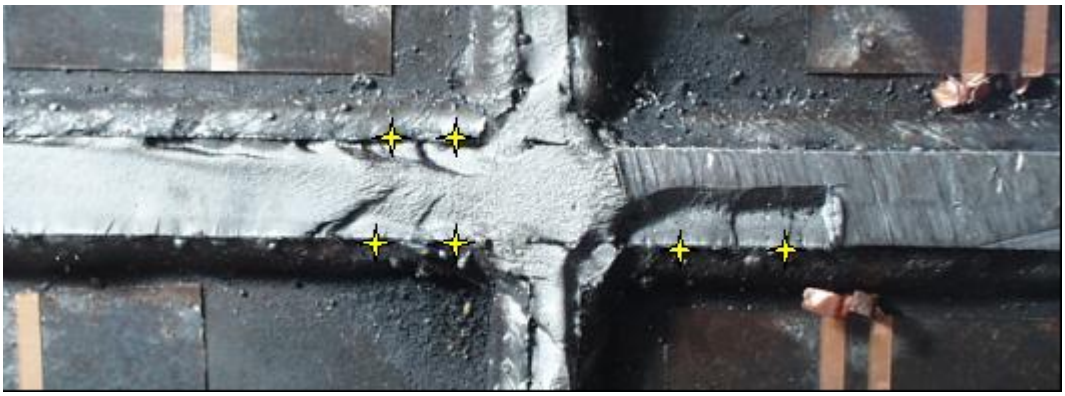

Figure 4-28: Center of Fracture Surface 11D-2

It is evident from the failures of all 12 specimens that undercutting had no impact on fatigue life. No specimens showed that cracks initiated at either a stiffener or flange undercut. Fracture surfaces of the specimens not shown above also support these findings.

4.3 DATA ANALYSIS

The results of the fatigue tests are evaluated in this section. The fatigue lives of the specimens were compared to the AASHTO nominal fatigue resistance category C' line. In addition, a single-factor analysis of variance (ANOVA) test was performed on the specimen groups using Microsoft Excel. The purpose of the data analyses is to (1) compare the AASHTO category C' nominal fatigue resistance to the resulting fatigue life of the specimens; and (2) to determine if there is a significant difference between the fatigue life of the type A, B, C, and D specimens due to stiffener geometry and undercutting caused by fully sealing the stiffener weld.

4.3.1 Comparison with AASHTO Fatigue Resistance

Figure 4-29 shows the results of the fatigue tests plotted along with the category C' nominal fatigue resistance line. The design fatigue life of the specimens is 550,000 cycles at a stress range of 20 ksi (138 MPa). The average fatigue life of all specimens tested was 452,533 cycles with an average measured stress range of 20.5 ksi (141 MPa).

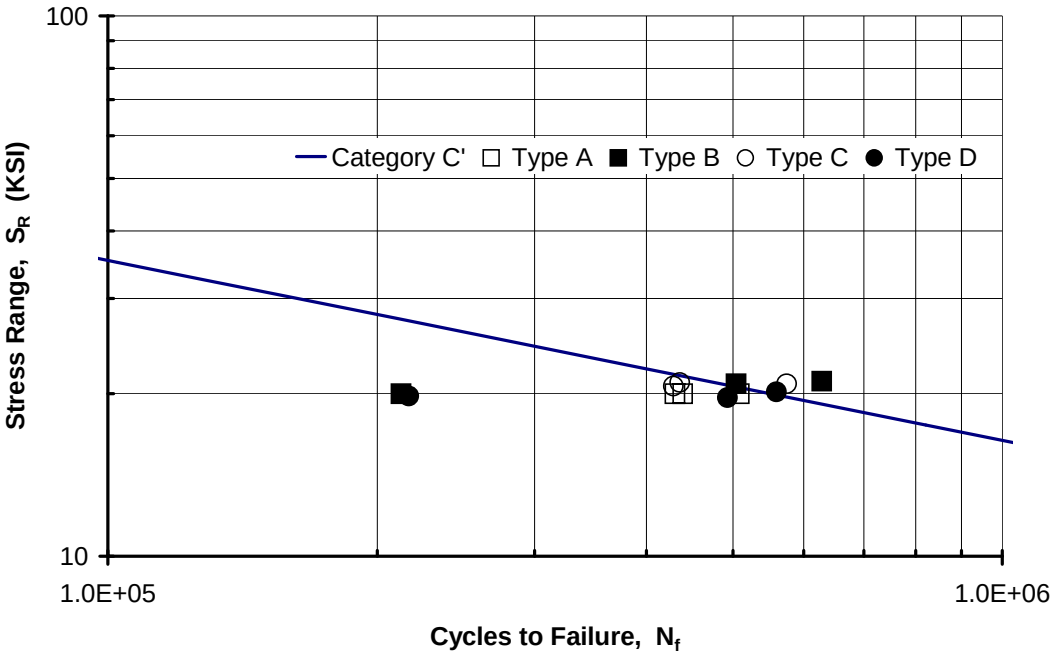

Figure 4-29: Comparison with Category C' Fatigue Resistance

The recorded stress range was higher than the nominal stress range at the stiffener connection. This may be one reason that average fatigue life of the specimens was lower than the predicted life. The fatigue life is a function of stress range in the following equation previously used in Chapter 2.2.

$$N_C = \left(44 \times 10^8\right) \cdot \left(S_{RC}{}^{-3}\right)$$

This is the equation of the C'-line shown in Figure 4-29. Table 4-3 lists the stress range and fatigue life of the experimental values in comparison to the AASHTO C'-line equation. Based on the minimum and maximum measured stress range of 19.7 ksi (136 MPa) and 21.1 ksi (145 MPa), the AASHTO nominal fatigue life ranges from 575,511 cycles to 468,388 cycles, respectively. At an average measured stress range of 20.5 ksi (141 MPa), the average fatigue life of specimens 1A through 12D was 452,533 cycles. This average is 15,855 cycles

lower than the minimum nominal fatigue life based on the AASHTO C'-line equation using a stress range of 21.1 ksi (145 MPa).

Table 4-3: Comparison of Actual and Predicted Fatigue Life

CASE	Stress Range S_R (ksi)	Cycles to Failure N_f
Average Test Results	20.5	452,533
AASHTO	19.7	575,511
Category C	21.1	468,388

Although the average fatigue life of the specimens is lower than the AASHTO C'-line prediction, it is believed that failure of the specimens was due to crack initiation at the stiffener-to-flange weld toe as established in section 4.2 of this chapter. The lower life is most likely due to the slightly higher and non-uniform stress in the flange plate and the larger stress concentration resulting from the stiffener on both sides of the flange.

4.3.2 Analysis of Variance

A single factor analysis of variance (ANOVA) was performed on the resulting fatigue lives of the type A, B, C, and D specimens. The analysis was used to compare the mean fatigue life of each specimen type to determine if they are significantly different or not significantly different. Findings from the analysis of variance indicated that there is no significant difference between the fatigue performance of the type A, B, C, and D specimens. The analysis was based on the assumption that differences in the measured stress range for each test specimen were irrelevant.

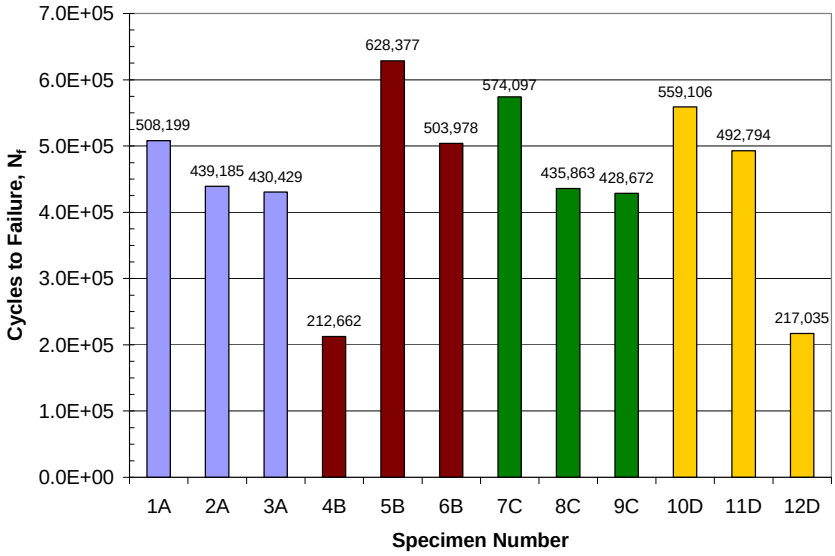

Figure 4-30: Specimen Fatigue Life

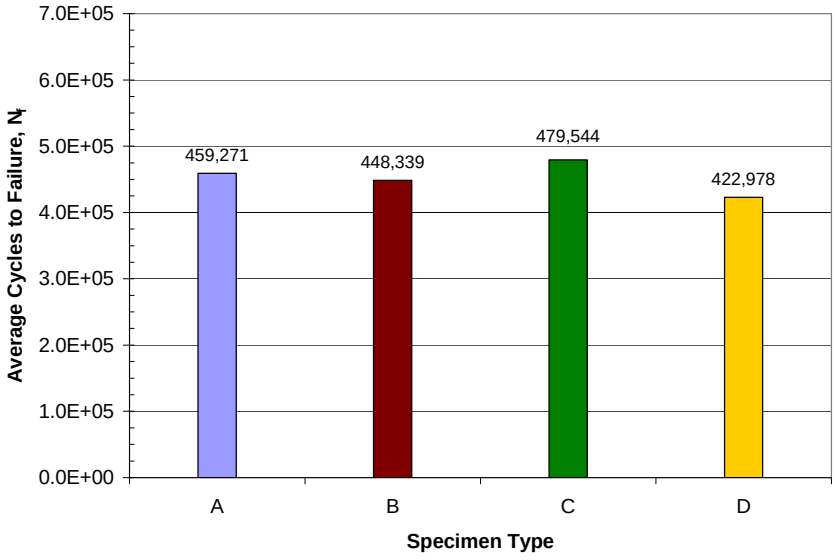

Figure 4-31: Average Fatigue Life by Specimen Type

Figure 4-30 shows a bar graph of the fatigue life of each specimen. The average fatigue life of all twelve specimens was 452,533 cycles. Figure 4-31 shows a bar graph of the average fatigue life of each specimen type. The average fatigue life of the type A, B, C, and D specimens was 459,271, 448,339, 479,544, and 422,978 cycles, respectively. The analysis of variance compares the mean life of each specimen type as well as the variance, or standard deviation, within and between each specimen type.

Table 4-4: Average Fatigue Life and Standard Deviation by Specimen Type

Specimen Type	Average Cycles to Failure	Standard Deviation
A	459,271	42,598
B	448,339	213,369
C	479,544	81,964
D	422,978	181,408

Table 4-4 summarizes the average fatigue life and standard deviation for the type A, B, C, and D specimens. The type C specimens had the longest mean fatigue life at 479,544 cycles. The Type D specimens had shortest mean fatigue life at 422,978 cycles. The difference between these fatigue life means is less than 12%. It can be seen from Figure 4-30 and Table 4-4 that the type A and type C specimens exhibit the least variance. The large standard deviation of the type B and D specimens is due to the short fatigue life of specimens 4B and 12D, respectfully. However, it should be noted that a thirteenth specimen was actually tested prior to specimen 12D. This additional type D specimen had lasted 292,583 cycles, more than the life of specimen 12D, prior to being inadvertently crushed due to a system failure triggered by a severe storm. There were no visible signs of cracking at the time of the accident. Specimen 12D was then fabricated to replace the damaged specimen.

The results of the analysis of variance are shown in Table 4-5. The analysis was performed on the fatigue life of the specimens, N_f, and the log of the fatigue life of the specimens, log N_f. A 95% level of significance ($\alpha = 0.05$) was used in the analyses.

Table 4-5: Analysis of Variance Results

ANOVA CASE	F	P-value	F crit
N_f	0.0766	0.971	4.07
$log\ N_f$	0.166	0.916	4.07

Several statistics were provided in the output table. However, F, Fcrit, and the P-value are of the greatest importance when interpreting the results. If F is greater than Fcrit, then there is a significant difference between the type A, B, C, and D fatigue life means. This would suggest that there was indeed an effect present. If F is not greater than Fcrit, then there is no significant difference between the type A, B, C, and D fatigue life means. Table 4-5 shows that F = 0.0766 is less than Fcrit = 4.07, indicating that there is no significant difference between the fatigue performance of the type A, B, C, and D specimens. It is also shown that there is no significant difference between the log fatigue lives of the specimens at the 95% level of significance.

However, if F was greater than Fcrit, the data fails the initial hypothesis that the means are equal. As a result, the alternate hypothesis that both means are significantly different gains more credibility. This is based upon the level of significance at which the analysis is performed. Denoted α, the most common level of significance used for an ANOVA is 95%, or $\alpha = 0.05$. The level of significance controls how stringently the mean values are compared, ultimately determining whether or not there is a significant difference in the fatigue life means. The P-value is the level of significance transitioning between a significant

outcome as opposed to an insignificant outcome. The P-value given in Table 4-5 is 0.971. Therefore, a level of significance (α) equal to this P-value would be needed to create an outcome indicating that there is a significant difference between the fatigue performance of the type A, B, C, and D specimens. In this case, using a level of significance of $\alpha = 0.971$ would be highly illogical, further supporting the hypothesis that there is no significant difference between the fatigue performances of the various specimen types.

CHAPTER 5
Summary and Conclusions

5.1 EVALUATION OF TEST RESULTS

It was found that wrapping the welds around the stiffener had no impact upon the fatigue life of the stiffener-to-flange connection. It is evident from the failures of all 12 specimens that undercutting at both the stiffener and flange had no impact on fatigue performance. No specimen failure indicated that cracks initiated at either a stiffener or flange undercut. Even the largest stiffener and flange undercuts, such as the ones shown in Figure 5-1, had no impact on fatigue life. All fatigue cracks initiated at the weld toe of the stiffener-to-flange weld.

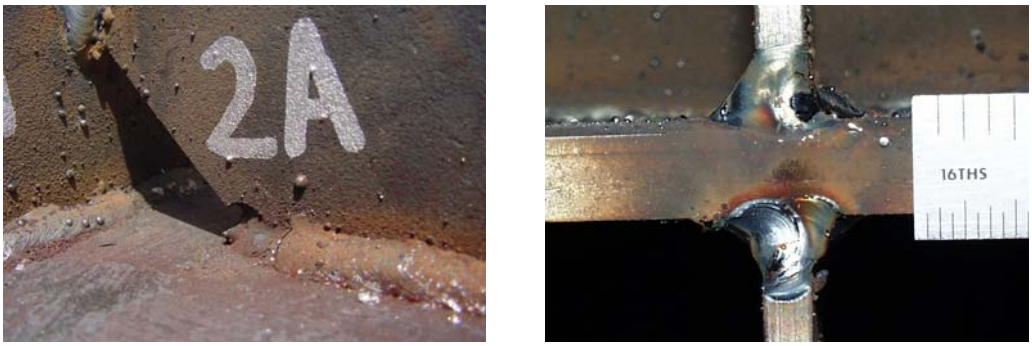

Figure 5-1: Stiffener and Flange Undercuts

Replicates of the four specimen types, defined A, B, C, or D, were tested at a nominal stress range of 20 ksi (138 MPa). The clip size of specimens A through C was 1.5 in. (38 mm). Specimen A stiffeners were stopped 0.625 in. (16 mm) short from the flange edge. Type B and C specimens had longer stiffeners extending completely to the edge of the flange. Flange undercuts on the type C specimens were repaired by grinding using the Bridge Welding Code D1.5-95

specifications. Type D specimens employed the shorter stiffener, and the clip size was reduced to 0.375 in. (9.5 mm) and welded shut. An analysis of variance was used to compare the mean fatigue life of each specimen type to determine if they are significantly different or not significantly different. Findings from the analysis of variance indicated that there is no significant difference between the fatigue performance of the type A, B, C, and D specimens.

5.2 RECOMMENDATIONS

Stiffener and flange undercuts were intentionally exaggerated during the welding process to produce worst-case scenarios. The average and maximum measured stiffener undercut values are listed in Table 5-1. The average and maximum measured flange undercut values are listed in Table 5-2. The average and maximum depths of the stiffener undercuts were 0.05 in. (1.2 mm) and 0.125 in. (3.2 mm). The average and maximum depths of the flange undercuts were 0.13 in. (3.3 mm) and 0.25 in. (6.4 mm).

Table 5-1: Stiffener Undercut Summary(inches)

Stiffener Undercuts	L	h	d
Avg.	0.058 (1.5 mm)	0.052 (1.3 mm)	0.047 (1.2 mm)
Max.	0.39 (10 mm)	0.35 (9 mm)	0.125 (3.2 mm)

Table 5-2: Flange Undercut Summary (inches)

Flange Undercuts	L	w	d
Avg.	0.57 (14.5 mm)	0.08 (2.0 mm)	0.13 (3.3 mm)
Max.	0.88 (22 mm)	0.25 (6.4 mm)	0.25 (6.4 mm)

The values listed in Table 5-1 and Table 5-2 are larger than measurements published in recent literature. In their study, Janosch and Debiez measured the average depth of undercutting at the weld toe. The largest average undercut depth reported was 0.03 in. (0.76 mm). Undercuts larger than 1 mm were typically rejected by weld inspectors (Iida et al., 1998).

With good welding practice, fillet welds can be wrapped around the stiffener with minimal undercutting as documented in the FHWA tour of steel bridge fabrication.

A 1.5 in. (38 mm) clip opening allowed adequate space to maneuver the welding gun to wrap the weld around the stiffener. Depending on the size of the web-to-flange welds, a clip size of 1.0 in. (25.4 mm) may be sufficient.

Research presented in this project showed that stiffener and flange undercuts do not impact fatigue life in the presence of flange forces. The effect of cross-frame forces in the stiffener upon the fatigue performance of the wrapped weld detail was not considered in this research. However, assuming that the stiffener forces are negligible, it can be restated that wrapping the weld around the stiffener has no impact upon fatigue life.

Bibliography

Massarelli, P. J., Baber, T. T. *Fatigue Reliability of Steel Highway Bridge Details.* Final Report, Virginia Department of Transportation and the University of Virginia. Commonwealth of Virginia, 2001.

Nussbaumer, A., Imhof, D. *On the Practical Use of Weld Improvement Methods.* Prog. Struct. Engng Mater, John Wiley and Sons, Ltd.Vol. 3, pp. 95-105, 2001.

Verma et al. *Steel Bridge Fabrication Technologies in Europe and Japan*. FHWA Report-PL-01-018, Washington, D.C.: The Federal Highway Association, March 2001.

AASHTO. *The AASHTO LRFD Bridge Design Specifications,* 2nd Edition. USA: American Association of State Highway And Transportation Officials, 1998.

AISC. *Manual Of Steel Construction, LRFD, 2nd Edition*. USA: American Institute of Steel Construction, 1998.

K. Iida et al. *Fatigue Strength of Butt-Welded Joint With Undercut.* Welding in the World, Vol. 39, No. 5, pp. 35-44, 1998.

Janosch, J.J., Debiez, S. *Influence of the shape of undercut on the fatigue strength of fillet welded assemblies, application of the local approach*. Welding in the World Vol. 41, No. 4, pp. 350-360, 1998.

Skaloud, M., Roberts, T.M. *Fatigue Crack Initiation and Propagation in Slender Webs Breathing Under Repeated Loading*. Journal of Construct. Steel Res., Vol. 46, No. 1-3, pp. 417-419, 1998.

Miki. C., Tateishi, K. *Fatigue Strength of Cope Hole Details in Steel Bridges*. International Journal of Fatigue, Vol. 19, No. 6, pp. 445-455, 1997.

Texas Department of Transportation. Fax Transmission: *CSTM-Structural, Fracture Critical Defect Repair Procedure #TI0003*. TxDOT, 1996. Fax Date: August 1, 2001.

ANSI, AWS, AASHTO. *Bridge Welding Code D1.5-95*. USA: American Welding Society and the State Highway And Transportation Officials, 1995.

Terasaki et al. *Effect of Undercut and Nonpropagating Crack Depths on Fatigue Strength of Welded Joint*. Journal Japan Institute of Metals, Vol. 58, No. 10, pp. 1149-1155, 1994.

Onozuka et al. *Fatigue Strength of Fillet Welded Joints with Undercuts*. Proceedings of the Third International Offshore and Polar Engineering Conference, Singapore, June 6-11, Vol. 4, pp. 199-205, 1993.

Skorupa, M., Scorupa, A. *Significance of Crack Initiation Period in Structural Steel Welds*. OMAE-ASME, Vol. III-B, pp. 715-720, 1993.

Petershagen, H. *The influence of undercut on the fatigue strength of welds, a literature survey*. Welding in the World, Vol. 28, No. 7/8, pp. 114-125, 1990.

Dijkstra et al. *The Fatigue Behavior of Welded Splices with and without Mouse Holes in IPE 400 and HEM 320 beams*. Weld Failures, November 1988.

Gurney, T. R. *Fatigue of Welded Structures, 2nd Edition*. Cambridge: Cambridge University Press, 1979.

The Lincoln Electric Company. *The Procedure Handbook Of Arc Welding, 12th Edition*. USA: The Lincoln Electric Company, 1973.

Gurney, T.R. *Effect of Peening and Grinding on the Fatigue Strength of Fillet Welded Joints*. British Welding Journal, December 1968.

Ruge, J., Woesle, H. *Results of Fatigue Investigations*, abstract of Ergebnisse von Dauerfestigkeitsuntersuchungen published in Die Schweisstechnik im Zeichen Neuzeitlicher Verfahren und Werkstoffe. Deutscher Verband fur Schweisstechnik, pp. 59-68, 1962.

Texas Department of Transportation. Plate Girder Details. Web Address: ftp://ftp.dot.state.tx.us/pub/txdot-info/cmd/cserve/standard/bridge/spgdstde.pdf 2001.